

Ensuring Medical AI Safety: Explainable AI-Driven Detection and Mitigation of Spurious Model Behavior and Associated Data

Frederik Pahde¹, Thomas Wiegand^{1,2,3}, Sebastian Lapuschkin^{1,†}, Wojciech Samek^{1,2,3,†}

¹Fraunhofer Heinrich Hertz Institut, Berlin, Germany

² Technische Universität Berlin, Berlin, Germany

³Berlin Institute for the Foundations of Learning and Data (BIFOLD), Berlin, Germany

[†]corresponding authors: {wojciech.samek,sebastian.lapuschkin}@hhi.fraunhofer.de

Abstract

Deep neural networks are increasingly employed in high-stakes medical applications, despite their tendency for shortcut learning in the presence of spurious correlations, which can have potentially fatal consequences in practice. Detecting and mitigating shortcut behavior is a challenging task that often requires significant labeling efforts from domain experts. To alleviate this problem, we introduce a semi-automated framework for the identification of spurious behavior from both data and model perspective by leveraging insights from eXplainable Artificial Intelligence (XAI). This allows the retrieval of spurious data points and the detection of model circuits that encode the associated prediction rules. Moreover, we demonstrate how these shortcut encodings can be used for XAI-based sample- and pixel-level data annotation, providing valuable information for bias mitigation methods to unlearn the undesired shortcut behavior. We show the applicability of our framework using four medical datasets across two modalities, featuring controlled and real-world spurious correlations caused by data artifacts. We successfully identify and mitigate these biases in VGG16, ResNet50, and contemporary Vision Transformer models, ultimately increasing their robustness and applicability for real-world medical tasks.

1 Introduction

In the past decade, Artificial Intelligence (AI) models have become ubiquitous in medical applications, often outperforming human experts in tasks like melanoma detection [14] and the prediction of cardiovascular diseases from electro cardiogram (ECG) data [68]. However, the non-transparent nature of

Deep Neural Network (DNN) predictions poses challenges in safety-critical contexts, as their reasoning remains obscure to both clinicians and model developers. This opacity is concerning, particularly since DNNs are prone to exploit spurious correlations in the training data. This can lead to shortcut learning [39], where models rely on (medically) irrelevant features, yet correlating with the target label. Such shortcuts are not limited to protected attributes like gender or ethnicity, but include various confounders in the training data, such as objects (*e.g.*, rulers or hair), color shifts, or watermarks added by scanning devices. A well-known example are band-aids in dermoscopic images for melanoma detection dominantly occurring beside benign lesions, causing AI models to associate the presence of band-aids with benign lesions with potentially severe consequences in practice. Similarly, DNNs trained to detect pneumonia from radiographs have predicted the hospital system used for the scan, as prevalence varied across hospitals in the study [78]. Moreover, confounding shortcuts were learned over intended signals from computed tomography scans for COVID-19 detection [23].

The field of XAI sheds light onto the previously non-transparent prediction behavior of DNNs, providing insights into their internal reasoning. While traditional local XAI methods focus on feature importance for individual predictions, global XAI approaches and mechanistic interpretability aim to understand overall model behavior by explaining the roles of internal representations and encoded features [1, 34, 79]. Recently, these insights have been utilized to systematically uncover model weaknesses like shortcut behavior. Current methods either detect outlier explanations for biased data samples [48, 3, 27] or outlier model concept representations [16, 53, 59]. Beyond revealing model weaknesses, XAI is also ca-

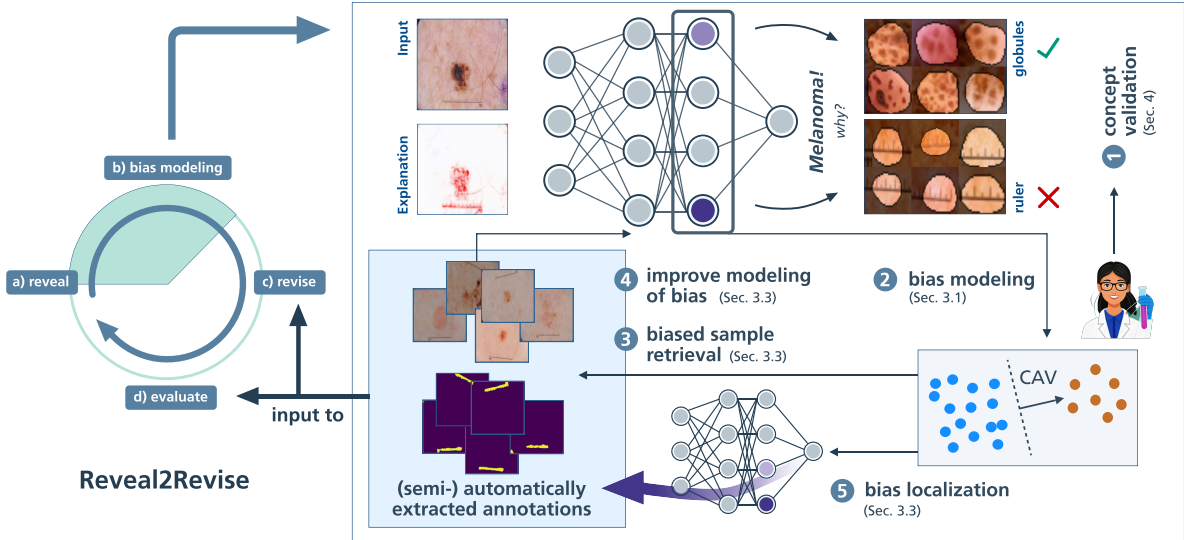


Figure 1: Extending the (a) reveal and (b) bias modeling steps of the Reveal2Revise framework, we demonstrate the power of XAI for bias detection, modeling, and data annotation. First, (1) bias identification approaches are leveraged to present outlier samples and concepts to model developers and domain experts for concept validation. Identified samples representing biases can be used for (2) bias modeling using CAVs. This bias representation can be utilized for (3) the retrieval of biased samples, which, in turn, can be used in an (4) iterative process to improve the bias representation. Revised bias representations are further used for (5) spatial bias localization. These semi-automatically extracted annotations are input to the (c) revise and (d) re-evaluation steps of Reveal2Revise.

pable of identifying data-related issues causing the undesired behavior. Most related to our work, the iterative Reveal2Revise framework [59] consists of the four steps (a) bias revealing, (b) bias modeling, *i.e.*, learning accurate bias representations, (c) model revision to unlearn shortcuts, and (d) re-evaluation. However, while it primarily focuses on model revision, it provides limited insights into bias revelation and modeling steps. This can lead to imperfect bias representations, limiting the effectiveness of the mitigation step. To fill this gap, we enhance the Reveal2Revise framework by providing a robust methodological foundation for the bias revelation and modeling steps to (semi-)automatically annotate and enrich datasets, leveraging insights from XAI, as illustrated in Fig. 1. Specifically, we discuss bias identification from both data and model perspectives, (1) enabling expert-guided validation of model behavior. Moreover, (2) we learn a model-internal bias representation, referred to as bias model, from an initial set of biased samples using Concept Activation Vectors (CAVs). We then (3) introduce the retrieval of biased data samples using the learned bias model, (4) enabling its iterative improvement. Furthermore, (5) using the refined bias model for spatial bias local-

ization, we enrich the dataset with extracted sample- and pixel-level annotations, which are used in the bias mitigation and evaluation steps of the Reveal2Revise framework to improve the generalization capabilities of AI models.

We demonstrate the applicability of our framework on four medical tasks across two modalities and provide annotations for the detected spurious concepts and data points¹. This includes image-based melanoma detection, the identification of gastrointestinal abnormalities, cardiomegaly prediction from chest radiographs, and cardiovascular disease prediction from ECG data using VGG, ResNet, and Vision Transformer (ViT) models. Utilizing our framework, we identify and mitigate both intrinsic and artificially introduced biases across all datasets, and demonstrate the data annotation capabilities using concept-based bias representations, minimizing the need for human supervision to improve the validity and robustness of AI models.

The paper is structured as follows: After summarizing related work in Sec. 2, we discuss how biases and concepts in general are modeled in DNNs

¹Both code and annotations are provided here: <https://github.com/frederikpahde/medical-ai-safety>

(Sec. 3.1), and leverage these representations for the (iterative) retrieval of biased samples (Sec. 3.2) and spatial bias localization (Sec. 3.3). We further discuss how (outlier) concepts and data points can be detected in the first place (Sec. 4), briefly describe bias mitigation methods (Sec. 5), and demonstrate the applicability of our framework in experiments (Sec. 6). Lastly, we discuss limitations and conclusions in Secs. 7 and 8, respectively.

2 Related Work

Existing XAI-based bias identification approaches primarily focus on shortcut detection in pre-trained models on benchmark datasets like ImageNet [24]. One line of research aims to identify samples with outlier model behavior, measured via local attribution scores in input [48] or latent [3, 27] space. Other methods seek to pinpoint spurious model representations like neurons or circuits directly. For instance, Singla and Feizi [66] employ human annotators to label neurons as valid or spurious using feature visualization techniques, leveraging this information to detect spurious samples. To minimize manual labeling, they consider only a subset of neurons based on their mutual information with model failures. In contrast to individual neurons, Neuhaus et al. [53] define class-wise neural Principal Component Analysis (PCA) to identify meaningful latent directions for each class, and leverage human annotators to label a pre-selected subset as spurious. With this approach they identify spurious features, such as the presence of bird feeders impacting the prediction of hummingbirds. Another recent bias identification method is Data-agnostic Representation Analysis (DORA) [16], which generates samples maximizing the neurons activations to represent concepts and defines a distance measure based on how neurons respond to representations of other neurons to identify outlier concepts. This has resulted in the identification of neurons extracting spurious concepts, such as watermarks or background features. In a medical context, existing works study shortcut behavior related to sensitive attributes like gender or age by comparing the model performance in different sub-populations [15], manually annotate the dataset for spurious features [9], or define heuristics to automate the detection of specific artifacts [62]. In contrast, our work presents a generic framework for the XAI-based identification of spurious correlations without prior knowledge and the (semi-)automatic generation of sample- and pixel-level annotations for spurious features. Closest to our work is Reveal2Revise [59], an iterative model

correction framework with the steps (1) *reveal* for bias identification, (2) bias modeling, (3) *revise* for bias mitigation, and (4) (re-)evaluation. While the Reveal2Revise framework emphasizes bias mitigation (step 3), our work extends and examines the XAI-based bias identification and modeling (steps 1 and 2) in greater detail, as well as its applicability for data annotation to reduce manual labeling efforts.

3 From Bias Modeling to (Semi-)Automated Data Annotation

In recent years, the XAI community has shifted its focus from local to global explanations to better understand overall model behavior. This line of research, known as *mechanistic interpretability*, aims to interpret internal representations in terms of human-understandable concepts, encoded as individual neurons, model circuits, or directions in latent space. Understanding model internals enables the identification of model substructures that encode biases stemming from data artifacts (step ② in Fig. 1). In this section, we discuss how biases are encoded within DNNs, and how this understanding can be utilized for data annotation tasks, such as the detection of biased samples and (spatial) bias localization. Note that while we assume knowledge on the existence of biases in this section, the identification thereof (step ① in Fig. 1) is addressed in Sec. 4.

Considered Types of Data Artifacts In this work, we focus on data artifacts caused by spurious correlations, *i.e.*, concepts unrelated to the (medical) task, yet correlating with the target label due to biases in the dataset curation process. Whereas some artifacts are entirely irrelevant to the task, *e.g.*, watermarks from medical devices, other artifacts can have a medical meaning but no causal impact on the predicted outcome, such as skin markers from dermatologists. We further distinguish between well-localized objects, such as band-aids or rulers, and non-localizable artifacts, *e.g.*, slight color or brightness shifts caused by the usage of different medical scanners. Data artifacts can spatially overlap task-relevant information, such that masking out artifactual regions might remove important information. Moreover, spurious features can be conceptually entangled with valid features. For example, in melanoma detection, model representations for specific color patterns indicative of lesions may be entangled with natural variations in skin tone.

3.1 Bias Modeling from an Explainable AI Perspective

We define a DNN as a function $f : \mathcal{X} \rightarrow \mathcal{Y}$ that maps input samples $\mathbf{x} \in \mathcal{X}$ to target labels $y \in \mathcal{Y}$. We further assume that at any layer l with m neurons, f can be split into a feature extractor $\mathbf{a}_l : \mathcal{X} \rightarrow \mathbb{R}^m$, computing latent activations at layer l , and a classifier head $\tilde{f} : \mathbb{R}^m \rightarrow \mathcal{Y}$, mapping latent activations to target labels. Neurons in layer l are denoted as \mathbf{n}_l^i with i indexing the neuron position in the respective layer. We further assume the existence of binary (bias) concept labels $t \in \{0, 1\}$.

Representing Concepts with Individual Neurons

Traditionally, it has been assumed that neurons in robust models encode human-aligned concepts, particularly at layers close to the model head [55, 61, 32, 6]. Hence, there might exist a neuron \mathbf{n}_l^i acting as feature extractor for a biased concept. Various feature visualization approaches aim to globally explain the concept represented by a neuron by identifying inputs that maximally trigger the neuron. Whereas one line of work generates inputs that maximally activate the selected neuron [33, 55, 35], other approaches select natural images from a reference dataset, *e.g.*, the training set. Specifically, while Activation Maximization (ActMax) [69, 11] selects samples that maximally *activate* a given neuron, Relevance Maximization (RelMax) [1] selects samples for which the neuron is maximally *relevant* for the classification task, as computed by a local explainability methods. In contrast to activations, the relevance scores are directly linked to the model prediction, indicating the neuron’s impact on a specified target label. However, limitations of the mapping of concepts to individual neurons are redundancy, *i.e.*, multiple neurons representing the same concept [25], and polysemanticity [38, 56, 31, 29], *i.e.*, neurons reacting to multiple, seemingly unrelated concepts. Recent works aim to overcome these challenges by *disentangling* learned concepts via Sparse Autoencoders (SAEs) [45, 13]. Assuming there are more concepts than neurons, SAEs leverage sparse dictionary learning to find an overcomplete feature basis, allowing the usage of encoder neurons as monosemantic concept representation.

Representing Concepts with Directions

Given the aforementioned limitations of neurons and the fact that there are typically more concepts than neurons, it is assumed that concepts are encoded as linear combinations of neurons, *i.e.*, directions in latent space, referred to as *superposition* [56, 31]. As an al-

ternative to disentangling the latent space via SAEs, these directions can be obtained directly, either in supervised or unsupervised fashion, as outlined below. Notably, using linear directions does not require knowledge on the role of neurons and allows the representation of *any* concept, even those not extracted by single neurons.

Supervised Concept Estimation: When concept labels t indicating the presence of a bias are known, concept directions can be estimated via Linear Probing [2, 7]. As such, CAVs, introduced for concept sensitivity testing [47], were originally computed as the weight vector $\mathbf{w} \in \mathbb{R}^m$ from a linear classifier like a linear SVM, distinguishing latent activations \mathcal{A}_l^+ on layer l of samples with the concept from activations \mathcal{A}_l^- of samples without it. However, recent work has shown that CAVs derived from linear classifiers can be influenced by distractors in the data, leading to inaccurate estimates of the concept *signal* direction [58]. The authors argue that maximizing class separability is the wrong optimization target and propose Pattern-CAVs, as detailed in Appendix A.1. CAVs can be computed on latent activations of arbitrary input shape, such as 3D representations of shape $C \times H \times W$, representing channel, height, and width dimensions, as well as aggregated representations. This includes translation-invariant 1D or channel-invariant 2D representations by using max- or average pooling over spatial or channel dimensions [50]. In this work, we use 1D-CAVs with max-pooling over spatial dimensions. Beyond linear concept representations, Concept Activation Regions have been proposed [21], allowing for non-linear concept representations through a radial kernel function.

Unsupervised Concept Discovery: When concept labels are not available, concepts can be discovered in unsupervised fashion. An early approach, Automatic Concept Extraction (ACE) [40], extracts concepts by segmenting images into regions and clustering similar regions to identify potential visual concepts. In contrast, recent approaches leverage matrix decomposition methods, such as PCA, Singular Value Decomposition (SVD), or Non-negative Matrix Factorization (NMF), on latent activations to identify meaningful directions in the model’s latent space [79, 34, 41, 53]. This leads to two matrices, with one matrix reinterpreted as the concept basis, *i.e.*, each row can be considered as CAV, and the other matrix as the activations within that new basis [36]. Another work proposes the discovery of linear subspaces as concept representations [72]. However, unsupervised concept discovery for representing data artifacts has two drawbacks: First, while no labeling efforts are needed to find concept labels, manual in-

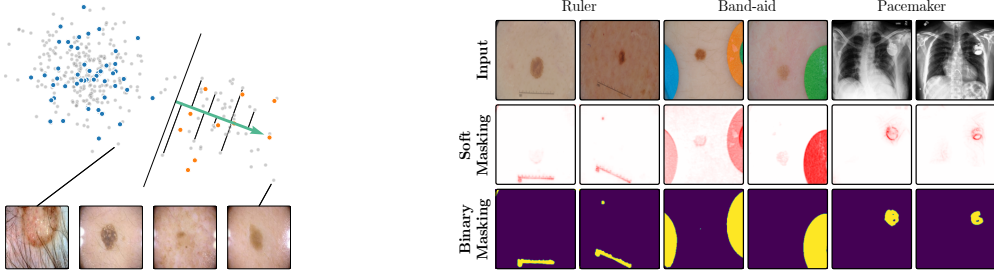


Figure 2: *Left*: Usage of a CAV encoding the **reflection** concept, trained on known artifact (●) and non-artifact (●) samples, for the annotation of unknown (●) samples. We rank samples by their bias score, computed by projecting their activation onto the CAV \mathbf{h}_l . *Right*: Localization of data artifacts by computing relevance heatmaps for the CAV \mathbf{h}_l for soft masking and their binarization.

spection is required to determine which direction(s) accurately represent the targeted concept, *i.e.*, the artifact to be modeled. Second, matrix factorization approaches yield statistical groupings without guidance without a guarantee for the existence of a direction representing the targeted artifact concept.

3.2 Biased Sample Retrieval

With a precise bias representation via CAV \mathbf{h}_l or neuron \mathbf{n}_l^i , the detection of artifactual samples can be further automated (step ③ in Fig. 1). Specifically, all samples from a dataset can be ranked by their similarity to the artifact representation, computed for example via cosine similarity, and presented to human annotators in that order, significantly supporting them in detecting artifact samples. Therefore, the data annotation process for concept representations based on a single neuron \mathbf{n}_l^i , as for example suggested by Singla and Feizi [66], is similar to global XAI methods explaining individual neurons via ActMax or RelMax, which retrieve reference samples with maximal activation or relevance for the given neuron. However, the limitations discussed above, namely redundancy and polysemanticity, affect the concept detection capabilities of individual neurons. To address this, extending the artifact representation to linear directions in latent space via CAVs is a viable solution. Specifically, given CAV \mathbf{h}_l and sample \mathbf{x} , we can compute a bias score $\mathbf{s}_{\text{bias}}^{\text{act}}$ by projecting latent activations $\mathbf{a}_l(\mathbf{x})$ for layer l onto the CAV:

$$\mathbf{s}_{\text{bias}}^{\text{act}} = \mathbf{h}_l^\top \mathbf{a}_l(\mathbf{x}) . \quad (1)$$

Alternatively, inspired by RelMax, we can compute bias scores using *relevance* scores instead of *activations*, as outlined in Appendix A.2. Since relevance scores are computed class-specifically, this approach allows distinguishing concepts that are artifactual for

certain classes but valid for others. An illustration is provided in Fig. 2 (*left*), where a CAV has been trained to distinguish between known artifact (●) and non-artifact samples (●). This concept representation can subsequently be used to compute concept scores $\mathbf{s}_{\text{bias}}^{\text{act}}$ for unknown samples (●), supporting annotators in the detection of further artifact samples.

Iterative Refinement of Bias Model Concept representations can be refined iteratively by correcting labeling errors in the data (step ④ in Fig. 1). Specifically, non-artifactual and unknown samples with *high* bias scores are subject to manual inspection to improve the label quality and concept representation, as shown in Fig. 3. Starting with ① a small set of bias samples obtained from bias identification methods, ② an initial CAV is fitted. Next, ③ manual inspection of samples with high bias scores improves the label quality. The updated labels are used to ④ iteratively refine the CAV, ⑤ resulting in a set of annotated bias samples.

3.3 Spatial Bias Localization

Beyond detecting artifact samples, XAI insights can further reduce human labeling efforts by automating the *spatial localization* of biased (and localizable) concepts within these samples (step ⑤ in Fig. 1). We assume the existence of a bias representation via CAV \mathbf{h}_l or neuron \mathbf{n}_l^i . The latter can be represented as CAV \mathbf{h}_l by setting all values to zero, except for the one for neuron \mathbf{n}_l^i , which is set to one. The targeted concept can then be localized in input space using local attribution methods, such as Layer-wise Relevance Propagation (LRP) [4]. Using singular neurons as concept representation, Singla and Feizi [66] leverage Class Activation Maps [80] to visualize the feature map for the given neuron in input space and

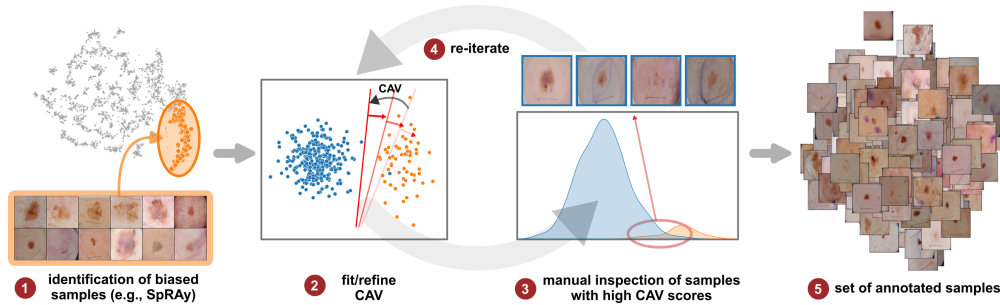


Figure 3: Iterative data annotation: (1) Given a small set of biased samples obtained via bias identification approaches, (2) a first CAV can be fitted. Using this CAV, (3) samples with high bias scores are subject to manual inspection to improve label quality. In an iterative process (4), CAVs are refitted, and the manual inspection is repeated, leading to an (5) improved set of annotated samples.

Achtibat et al. [1] mask latent relevances for local attribution methods to compute neuron-specific input heatmaps. This approach can be extended to biases represented as direction in latent space, *e.g.*, using PCA [53] or CAVs [3, 59, 22]. Specifically, given the concept direction \mathbf{h}_l and latent activations $\mathbf{a}_l(\mathbf{x})$, we can utilize local explanation approaches like LRP [4] to explain the prediction of the function producing the bias score $s_{\text{bias}}^{\text{act}}$ as defined in Eq. 1. This is equivalent to a local attribution method applied to sample \mathbf{x} , with latent relevance scores $\mathcal{R}_l(\mathbf{x})$ initialized as

$$\mathcal{R}_l(\mathbf{x}) = \mathbf{a}_l(\mathbf{x}) \circ \mathbf{h}_l \quad (2)$$

where \circ denotes element-wise multiplication. This yields a heatmap that can be used as a soft mask or converted to a binary segmentation mask, for instance using thresholding techniques like Otsu’s method [57]. An example is shown in Fig. 2 (*right*), showing soft masks as heatmaps from concept-conditioned local attribution scores, along with binary masks for three known data artifacts: rulers and band-aids for skin cancer detection, and pacemakers in chest radiographs.

Notably, automated bias localization has the potential to reduce manual annotation efforts. These additional annotations can be utilized for various applications, *e.g.*, as input for bias mitigation approaches requiring prior information on the bias to be unlearned (see Sec. 5). Other applications include the design of metrics to measure artifact reliance or the spatial isolation of the bias to copy-paste it onto non-artifactual samples to measure the model’s sensitivity is towards the insertion of the artifact [59].

4 Concept Validation: Detecting Spurious Behavior

Given the large number of model parameters, detecting biased model representations can be like searching for a needle in a haystack, especially without prior knowledge of spurious correlations. To address this challenge, a common strategy is to identify outlier model behavior using a reference dataset. Automated detection approaches typically focus on either analyzing post-hoc explanations for a set of reference images to find anomalous model behavior [48, 27] or identifying outlier representations within the model itself [16, 53]. For concept validation (step (1) in Fig. 1), we distinguish between the *data perspective* in Sec. 4.1, which focuses on detecting samples exhibiting outlier behavior, and the *model perspective* in Sec. 4.2, which aims to identify outlier concept representations within the model. However, it is to note that outlier model reasoning is not necessarily caused by spurious correlations, but can be (clinically) valid model behavior that is rarely used. Thus, detecting spurious correlations often requires manual inspection by human experts to determine whether outlier behavior is valid or caused by spurious correlations.

4.1 Data Perspective – Detecting Spurious Samples

A first line of works assumes that models use a different behavior for spurious samples compared to “clean” samples. Concretely, model behavior can be estimated using local attribution methods, such as Input Gradients [51, 65], GradCAM [64], or LRP [4]. Note, that backpropagation-based attribution approaches distribute relevance scores from the output through all layers to the input, enabling the analysis of both *input* heatmaps and *latent* relevance scores.

This allows the analysis of prediction behavior at different abstraction levels, represented as relevance scores $\mathcal{R}_l \in \mathbb{R}^{N \times C \times H \times W}$ for N samples in layer l with C channels and spatial dimension $H \times W$, or (spatially) aggregated representations. Using a distance function, such as cosine distance, we compute a pairwise distance matrix $\mathcal{D}_l \in \mathbb{R}^{N \times N}$ for further inspection.

Analyzing Input Heatmaps Spectral Relevance Analysis (SpRAy) groups input heatmaps using spectral clustering to identify outlier explanations that are likely to stem from spurious correlations [48]. This technique has uncovered various spurious correlations, such as the influence of photographers’ watermarks for horse detection or other artifacts. However, it is limited to well-localized biases that result in high relevance in similar spatial locations.

Analyzing Latent Relevance These limitations can be mitigated by applying SpRAy to relevances in *latent* space [3]. Conveniently, many local attribution methods backpropagate relevance scores from the model output to the input, yielding scores for each neuron that indicate the importance of features extracted by those neurons. Applying SpRAy allows clustering of latent relevance scores to identify typical and atypical model behavior, as shown in clinical gait analysis [67]. Note, that the clustering can be performed using relevance scores of shape $H \times W \times C$, as done by Anders et al. [3], or in spatially aggregated manner using max- or average-pooling. For example, Prototypical Concept-based eXplanations (PCX) [27] train Gaussian Mixture Models on max-pooled latent relevance scores and consider cluster means as stereotypical explanation, encoded as distribution over concepts (*i.e.*, neurons).

Both input and latent relevance clustering require subsequent human supervision to determine whether outlier clusters represent valid or spurious behavior. To semi-automate this process, Anders et al. [3] propose using Fisher Discriminant Analysis [37] to rank class-wise clusterings by linear separability, while Dreyer et al. [27] computes similarities between prototypes. The results of clustering approaches can serve as an initial set for bias modeling methods outlined in Sec. 3.2, which can be refined iteratively. An example outlier cluster of latent relevances is shown in Fig. 4 (*top*), with all samples containing the spurious band-aid concept.

4.2 Model Perspective – Detecting Spurious Representations

In contrast to detecting spurious *samples*, recent work focuses on identifying spurious *model internals* directly. This aligns with mechanistic interpretability, which seeks to decipher the internal mechanics of DNNs [56, 31, 13]. As outlined in Sec. 3.1, various global XAIs methods aim to explain the role of individual neurons, and these insights can be leveraged to detect spurious model internals by clustering learned concepts and identifying outliers. Given input data \mathcal{X} with N samples, Pahde et al. [59] compute spatially aggregated relevances $\mathcal{R}_l \in \mathbb{R}^{N \times C}$. Subsequently, they compute the pairwise cosine distance per column (*i.e.*, channel/concept) and embed the resulting distance matrix $\mathcal{D}_l \in \mathbb{R}^{C \times C}$ in a low-dimensional space using dimension reduction techniques like t-Distributed Stochastic Neighbor Embedding (t-SNE) [71] or Uniform Manifold Approximation and Projection (UMAP) [49]. This low-dimensional embedding can be visualized to identify outliers through human inspection or anomaly detection algorithms, such as the Local Outlier Factor [12]. In summary, outlier representations can be identified in an embedding representation $E \in \mathbb{R}^{C \times L}$, obtained as

$$E = \text{emb}(d_p(\mathcal{D}_l)) \quad (3)$$

where $\text{emb} : \mathbb{R}^{C \times C} \rightarrow \mathbb{R}^{C \times L}$ reduces the dimension to L , and the pairwise distance function $d_p(\cdot)$ is applied along all channel dimensions in the latent representation \mathcal{D}_l , either given by activations or relevance scores for layer l . Note that this approach assumes over-parameterization resulting in redundant neurons, allowing to distinguish between similar and dissimilar concept representations. An example is shown in Fig. 4 (*bottom*), where latent relevance scores from a ResNet50 model trained for melanoma detection are used to identify outlier concepts, specifically a cluster focusing on band-aids rather than clinically relevant features. Notably, Eq. 3 can easily be extended to find outlier *directions* instead of neurons. Specifically, this involves a linear transformation of latent representations \mathcal{D}_l using the directions of interest, *e.g.*, obtained in unsupervised manner as described in Sec. 3.1.

Similarly, DORA embeds a pairwise distance matrix of neuron representations into 2D, but proposes a data-agnostic approach and a tailored distance function [16]. Specifically, they generate ActMax samples as concept representation for neurons, referred to as natural Activation-Maximization signals (n-AMS). Each neuron \mathbf{n}_i^j is represented by a representation activation vector $r_i \in \mathbb{R}^C$, measuring how much *other*

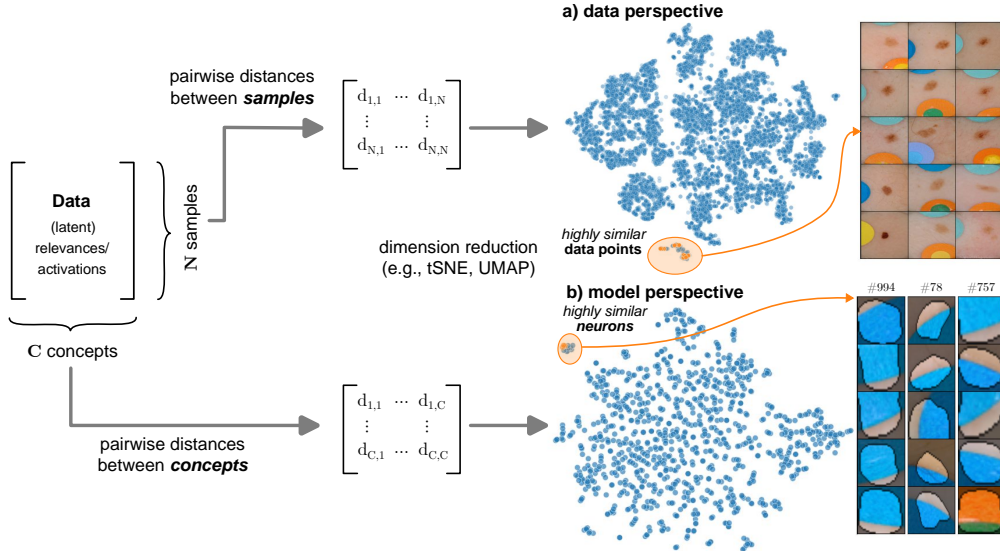


Figure 4: Spurious correlations are identified by detecting outliers in model behavior. This involves computing pairwise distances of (latent) activations or relevances from either the data (*top*) or model (*bottom*) perspective. The resulting $N \times N$ (data perspective) or $C \times C$ (model perspective) distance matrix is then reduced to 2D for visualization and outlier detection. Human annotators determine whether detected outliers pose spurious correlations or valid prediction behavior.

neurons activate on the given n-AMS, and compute pairwise distances between the vectors. The resulting distance matrix $\mathcal{D}_l \in \mathbb{R}^{C \times C}$ is embedded into lower dimension to identify outlier representations. Notably, instead of generating ActMax samples, this approach can also be applied on *real* samples from a reference dataset.

Lastly, Neuhaus et al. [53] use human supervision to identify spurious concepts represented as linear directions in latent activations obtained via PCA. To reduce manual labelling efforts, they propose an automated pre-selection of concept representations by focusing on the top 128 PCA components and raking them based on the model’s confidence in classifying reference samples in the given direction. Another promising direction is auto-labelling neurons, *e.g.*, via foundation models, to search for expected valid or spurious concepts and to analyze unexpected concepts [44, 54, 30, 17].

5 Bias Mitigation

After detecting model biases and identifying biased samples, we aim to unlearn undesired behaviors through bias mitigation. A first line of approaches modifies the training data, *e.g.*, by removing or manipulating biased samples, followed by retraining the model [77, 75]. While effectively mitigating biases,

this method requires access to the full training set, can be costly, and may ignore valuable information, leading to practical limitations. In an iterative model development life cycle like Reveal2Revise, with continuous model validation and bias mitigation, full retraining is often infeasible. Thus, we focus on efficient bias mitigation approaches, that either finetune the (biased) model with a custom bias mitigation loss function or modify the model post-hoc without additional training. As such, Right for the Right Reason (RRR) [63] penalizes the alignment between the input gradient, *i.e.*, the gradient of the prediction w.r.t. the input features, and ground truth masks localizing the artifact. Note, that this approach requires pixel-wise annotations for bias localization, which can be costly. However, (semi-)automated data annotation techniques outlined in Secs. 3.2 and 3.3 can reduce the manual effort.

As an alternative to input-level bias representations, the Class Artifact Compensation (ClArC) framework [3] models biases in latent space using CAVs, requiring only binary labels per sample to indicate the presence of the artifact. Inspired by RRR, Right Reason ClArC (RR-ClArC) [28] penalizes the feature use measured by the *latent* gradient pointing into the direction of the bias, as modeled via the CAV. Another research direction is training-free post-hoc model editing [3, 53, 8]. For instance, Projective ClArC (P-ClArC) [3] removes activations in the

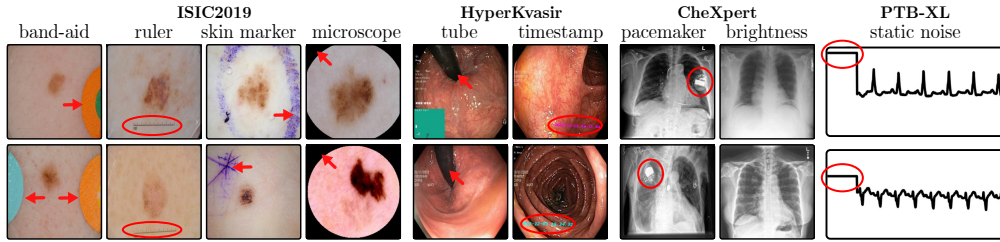


Figure 5: Examples for considered artifacts (f.l.t.r.): We use the real-world artifacts **band-aid**, **ruler**, and **skin marker** for ISIC2019, and an artificially inserted **microscope**-like black circle. In Hyper-Kvasir, we use **insertion tubes** and artificial **timestamps**. For CheXpert, we consider **pacemakers** and artificially increased **brightness**. Lastly, we insert **static noise** into one lead in PTB-XL.

bias direction modeled via CAVs during the prediction. However, bias mitigation approaches risk “collateral damage”, meaning that whereas the biased concept is successfully suppressed, valid concepts entangled with the biased concept might be negatively impacted as well. To address this, reactive P-ClArC (rP-ClArC) [5] only targets samples meeting certain conditions, such as containing the artifact according to the CAV. A detailed description of bias mitigation approaches is provided in Appendix A.3.

6 Experiments

We evaluate our framework with four medical datasets from two modalities, namely vision and time-series. After describing the experimental setup (Sec. 6.1), we demonstrate the capabilities of our framework for bias identification (Sec. 6.2), the detection of biased samples (Sec. 6.3), bias localization (Sec. 6.4) and mitigation (Sec. 6.5).

6.1 Experimental Setup

The considered datasets include ISIC2019 for melanoma detection [19, 70, 20], HyperKvasir for the identification of gastrointestinal abnormalities [10], CheXpert with chest radiographs [46], and the PTB-XL dataset [73] with 12-lead ECG (time series) data. All vision datasets contain real-world artifacts that DNNs may utilize as spurious correlation, *i.e.*, features unrelated to the task, yet correlating with the target label. ISIC2019 is particularly known for various artifacts like colorful **band-aids** near benign lesions and **rulers** or **skin markers** beside malignant lesions [62, 3, 18, 59]. Moreover, HyperKvasir contains **insertion tubes** predominantly in samples without abnormal conditions, while CheXpert samples with cardiomegaly contain **pacemakers** in radiographs more frequently than in healthy patients [75].

In addition, we insert controlled artifacts into a subset of images from exactly one class per dataset. Specifically, we insert a **microscope**-like artifact into melanoma samples in ISIC2019. Moreover, following Dreyer et al. [28], we insert a **timestamp** into disease-samples from HyperKvasir, mimicking timestamps added by scanning devices. For CheXpert, we increase the **brightness** of radiographs with cardiomegaly, while for PTB-XL, we insert a **static noise** into the first second of one lead for samples with left ventricular hypertrophy (LVH). Inserting these artifacts into $p\%$ of samples from exactly one class creates spurious correlations for that class. Further dataset details are provided in Appendix A.4 and examples of the artifacts are shown in Fig. 5.

Model Details: For vision tasks, we use VGG16 [65], ResNet50 [42], and ViT-B-16 [26] model architectures with checkpoints pre-trained on ImageNet [24] obtained from the PyTorch model zoo [60] and timm [76]. For ECG data, we utilize a one-dimensional adaptation of XResNet50 [43], following recent benchmarks [68, 74]. We replace the last linear layer to match the number of classes and finetune the models with training details and model performance reported in Appendix A.5.

6.2 Concept Validation: Identification of Spurious Behavior

Given the fitted models, we apply bias identification methods introduced in Sec. 4 to detect the expected spurious model behavior. Throughout this section, we focus on the ResNet50 model trained on ISIC2019 with various confounders. We further limit our analyses to samples from the melanoma class to prevent that clustering model behavior results in clusters representing different classes, and instead allowing us to identify spurious sub-strategies for predicting the considered class.

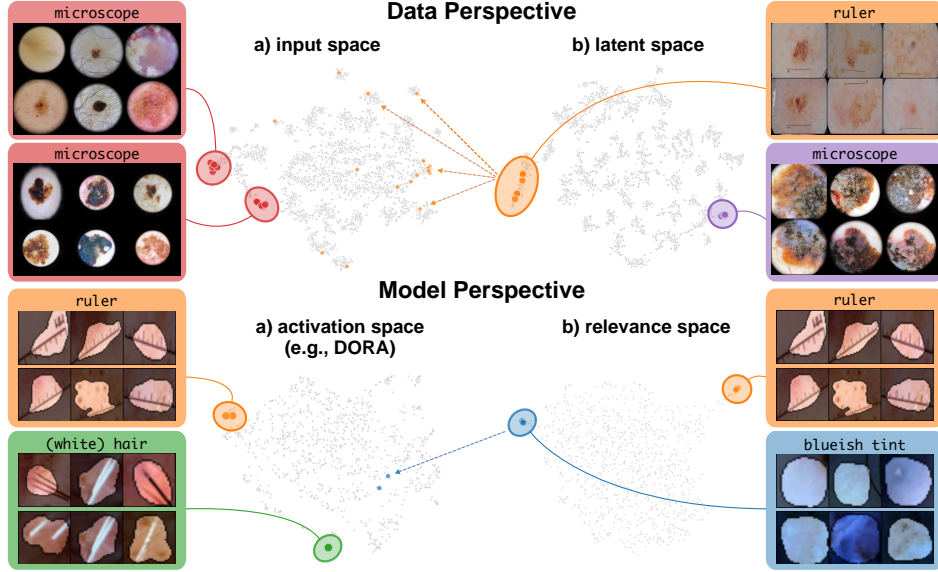


Figure 6: Detected outlier behavior for the prediction of melanoma using a ResNet50 model trained on ISIC2019. *Top*: Bias identification methods from the data perspective, specifically SpRAY on input (*left*) and latent (*right*) relevance scores. *Bottom*: Bias identification methods from the model perspective, specifically concept clustering with activation pattern using DORA (*left*) and with relevance pattern via cosine similarity (*right*), reveal various bias concepts, *e.g.*, ruler structures or hair.

Data Perspective We first apply SpRAY in input and latent space, computing input feature importance scores using LRP summed over color channels. To obtain latent relevances, we use intermediate relevance scores in the LRP computation process after the 3rd (out of four) residual block, max-pooling over spatial dimensions to yield relevance scores $r_l \in \mathbb{R}^C$ for layer l with C channels. The clustering of pairwise cosine distances between heatmaps is shown in Fig. 6 (*top left*). Detected outlier clusters contain samples with spatially coherent biases, *e.g.*, the black circle around the lesions originating from **microscopes** (●). In contrast, clustering latent relevance scores reveals more complex, less spatially dependent clusters, as shown in Fig. 6 (*top right*), including the **ruler** artifact (●) and the **microscope** (●). Compared to those in input space, the cluster for the **microscope** in latent space represents a more diverse high-level concept. In the input space visualization, we further highlight samples from the **ruler** cluster detected in latent space. Instead of forming a cluster, they spread across the entire embedding space, indicating that the bias is too complex to be detected in input space.

Model Perspective Next, we apply bias identification approaches from the model perspective by identifying outlier neurons based on *activation* pattern via DORA and *relevance* pattern by clustering

pair-wise cosine distances between concept relevance scores. We focus on latent activations and relevances after the third residual block. DORA uses a distance function based on how neurons activate upon each others n-AMS, achieving high similarity when neurons activate upon similar input signal. A 2D visualization of the resulting distance matrix is shown in Fig. 6 (*bottom left*). Identified outlier concepts include **ruler** (●) and **(white) hair** (●). We further compute pairwise cosine distances between latent relevance scores $r_l \in \mathbb{R}^{N \times C}$, aggregated over spatial dimensions, and apply UMAP to embed the resulting distance matrix $D_l \in \mathbb{R}^{C \times C}$ in $\mathbb{R}^{C \times 2}$. This results in high similarity between neurons (concepts) that the model uses similarly for predictions. The concept clustering is visualized in Fig. 6 (*bottom right*), highlighting two outlier clusters focused on **rulers** (●) and **blueish tint** (●).

Results for other classes, model architectures, and datasets are presented in Appendix A.6.1. This includes experiments with ECG data in Fig. 10, revealing the artificially inserted **static noise** in the attacked lead from both data and model perspectives. Notably, dominant spurious concepts, such as the artificial **timestamp** in HyperKvasir or the **static noise** in PTB-XL, may not be detected as *outlier* concepts. In such cases, analyzing prediction sub-strategies via PCX may provide additional insights on

spurious *inlier* behavior. Hard-to-interpret concept representations pose another challenge for the model perspective. For example, the **brightness** artifact in CheXpert is not clearly visible in the concept UMAP (see Fig. 15, *right*), but can easily be detected using SpRAy (Fig. 15, *left*) or PCX (Fig. 22). In summary, while all considered spurious features are detected, the choice of bias identification approach is crucial, as some shortcuts are easier to detect as outlier concept (*e.g.*, **ruler**) and others via PCX (*e.g.*, **brightness**, **static noise** in ECG).

6.3 Biased Sample Retrieval

In this section, we leverage latent bias representations, either via directions or individual neurons, to retrieve biased samples and measure how well bias samples are separated from clean samples. We compute bias scores $s_{\text{bias}}^{\text{act}}$ as defined in Eq. 1 by projecting latent activations onto the bias direction. As we are mostly interested in the ranking capabilities, *i.e.*, artifact samples should be assigned higher bias scores than clean samples, we measure Area Under the Receiver Operating Curve (AUROC) and Average Precision (AP), considering both real and controlled artifacts. For real artifacts, we evaluate retrieval using existing artifact labels, while we have ground truth information for controlled experiments. We train CAVs using Support Vector Machines (SVMs) on different layers of VGG16 and ResNet50 models for all datasets, reporting AUROC and AP on unseen test samples. Note, that while Pahde et al. [58] claim that classifier-based CAV computation can yield imprecise concept directions, they argue that SVM-CAVs are superior for predicting concept presence, the main goal of this experiment. In Fig. 7, we show the results for different layers of VGG16 and ResNet50 using single neurons (dashed line) and CAVs (solid line) as bias representation. Best neurons are selected using the validation set. The results indicate that CAVs generally outperform single neuron representations for sample retrieval, and the layer choice is crucial depending on the bias type. For instance, while CAVs for layers closer to the model heads can detect **pacemaker** samples, they fail for earlier layers.

We further plot the distribution of CAV-based bias scores for biased and clean samples for the real-world artifacts **ruler** (ISIC2019) and **pacemaker** (CheXpert) in Fig. 8. We compute bias scores using the best performing CAV per artifact and use latent activations after the 3rd residual block of the ResNet50 model for **ruler**, and the 10th convolutional layer of the VGG16 model for **pacemaker**. We show samples corresponding to the bias score in the top-1 and -99

percentiles of each set. Samples near the decision boundary are particularly interesting, as they may arise from labeling errors. Both examples demonstrate the retrieval of unlabeled artifact samples. The distributions of bias scores for additional artifacts are shown in Appendix A.6.2.

6.4 Spatial Bias Localization

To spatially localize biases in input space with CAVs, we compute local explanations for the element-wise product of latent activations \mathbf{a} and concept direction \mathbf{h}_l (see Eq. 2). We use the controlled artifacts, specifically **timestamp** (HyperKvasir) and **microscope** (ISIC2019) with ground truth concept localization masks for evaluation. We compute (1) the percentage of relevance *within* the ground truth mask and (2) the Jaccard index, or Intersection over Union (IoU), of the binarized localization mask with the ground truth. In Fig. 9, we report both metrics using CAVs computed on different layers of VGG16 and ResNet50. The layer choice for concept representations is key, as for example middle layers perform better to localize **timestamps** and earlier layers are more effective to localize the **microscope**. In comparison with Fig. 7, we find that the optimal layer for bias localization may differ from the one for sample retrieval. Interestingly, the IoU for the **microscope** artifact is consistently low, as models primarily focus on the border of the circle instead of the entire area, as indicated by qualitative results in Appendix A.6.3. Unlike artifact relevance, the IoU metric also measures how much of the expected areas the computed mask does *not* cover.

6.5 Bias Mitigation

We unlearn detected biases using the methods summarized in Sec. 5. We utilize RRR as input-gradient-based bias mitigation approach for localizable artifacts and the ClArC framework for all artifacts, representing biases in latent space with CAVs. Specifically, we consider the penalty-based approach RR-ClArC and the training-free model editing methods P-ClArC and rP-ClArC. To measure the bias mitigation effect, we compute several metrics inspired by prior work [59]. First, we compare the accuracy on a clean (bias-free) and a biased test set, where the bias is artificially inserted into samples from all classes. Models impacted by spurious correlations are expected to perform poorly on the biased test set. In addition, we measure the model’s sensitivity towards the bias concept by computing (1) the percentage of relevance, measured via LRP, on the artifact region us-

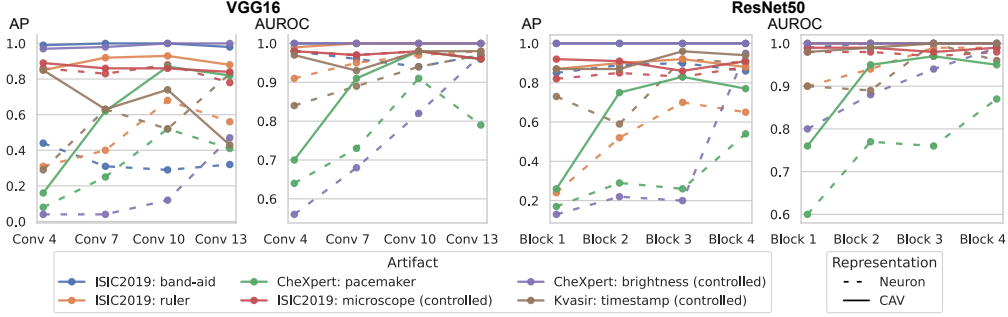


Figure 7: Quantitative data annotation results measuring the ranking capabilities via AP and AUROC for different layers of VGG16 (*left*) and ResNet50 (*right*) using artifacts from ISIC2019 (band-aid, ruler, microscope), HyperKvasir (timestamp) and CheXpert (pacemaker, brightness). As concept representation, we use single neurons (*dashed*) and CAVs (*solid*).



Figure 8: Distribution of latent activations projected onto CAV direction for known artifacts ruler ISIC2019 (*left*) and pacemaker in CheXpert (*right*), split into known artifact (*orange*) and other (*blue*) samples. We show samples at the 1- and 99-percentile of each set and the artifact localization using CAVs. In both cases, the samples in the 99-percentile of the set *not* labeled as artifact are false negatives, i.e., artifact samples that have not been detected in the data annotation process.

ing ground truth masks, and (2) the TCAV score [47]. The latter is reported as $\Delta\text{TCAV} = |\text{TCAV} - 0.5|$, where 0 indicates no sensitivity and higher values reliance on the artifact. Low scores are preferred after bias mitigation. The results are compared to a Vanilla model that is finetuned without a bias mitigation loss term. In Tab. 1, we report results for ResNet50 models in the controlled settings with ISIC2019, HyperKvasir, and CheXpert. For RRR, we use ground truth bias localization masks and refrain from reporting results for CheXpert, as we consider the **brightness** artifact unlocalizable in input space. The results confirm that all models initially rely on the spurious correlation, indicated by a large gap between clean and biased accuracies for Vanilla models. All bias mitigation approaches improve the accuracy on the biased test set while maintaining high accuracy on the clean test set, demonstrating reduced reliance on the targeted biases. This is supported by decreased artifact relevance and ΔTCAV . Qualitative results visualizing the decrease in artifact reliance with input relevance heatmaps and additional quantitative results for other model architectures and ECG data are provided in Appendix A.6.4.

7 Limitations

While all steps in our framework are semi-automated, they require human supervision from domain experts, *e.g.*, to validate outlier concepts, inspect detected bias samples, and determine which concepts should be unlearned. Below, we discuss additional challenges associated with each step of our framework.

- *Concept Validation/Bias Identification:* When encoded biases dominate, they may not appear as outlier concepts or samples. Identifying prediction sub-strategies, *e.g.*, using PCX, can overcome this challenge. Moreover, it is to note that if the discussed approaches are not applied per class label, detected clusters might resemble clusters of classes instead of different sub-strategies.
- *Bias Modeling:* Without explicit concept disentanglement (*e.g.*, via SAEs), concept representations may be non-orthogonal, leading to entangled concepts that negatively impact data annotation and bias mitigation. An additional limitation poses the linear separability assumption of CAVs, as there is no guarantee for the

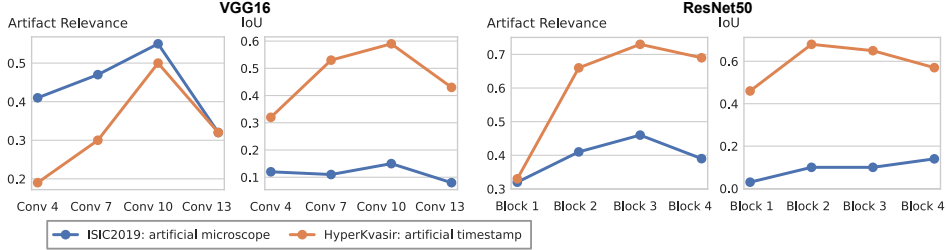


Figure 9: Bias localization results measuring the artifact relevance and IoU for various layers of VGG16 and ResNet50 using our controlled artifacts `microscope` (ISIC2019) and `timestamp` (HyperKvasir).

Table 1: Bias mitigation results with RRR, RR-ClArC, and P-ClArC (plain and reactive) for ResNet50 models for controlled spurious correlations, specifically ISIC2019 (`microscope`) | HyperKvasir (`timestamp`) | CheXpert (`brightness`). We report accuracy on a clean and biased test set, artifact relevance and Δ TCAV and arrows indicate whether high (\uparrow) or low (\downarrow) are better.

Method	Accuracy (clean) \uparrow			Accuracy (biased) \uparrow			Art. relevance \downarrow			Δ TCAV \downarrow		
<i>Vanilla</i>	0.87	0.97	0.81	0.28	0.62	0.44	0.55	0.51	-	0.17	0.30	0.33
RRR	0.84	0.97	-	0.51	0.82	-	0.53	0.45	-	0.19	0.30	-
RR-ClArC	0.86	0.97	0.82	0.76	0.96	0.79	0.42	0.34	-	0.00	0.07	0.00
P-ClArC	0.82	0.83	0.72	0.59	0.92	0.76	0.44	0.18	-	0.07	0.11	0.30
rP-ClArC	0.87	0.97	0.81	0.60	0.92	0.76	0.42	0.19	-	0.07	0.11	0.30

existence of a layer perfectly separating concept samples. This makes the layer selection an additional hyperparameter, and a suboptimal choice can exacerbate issues like concept entanglement. Non-localizable artifacts (*e.g.*, color shifts) are another challenge, as they cannot be effectively modeled using spatial masks in input space. Lastly, poorly chosen data samples representing the concept can limit the accuracy of bias representations.

- *Bias Localization:* Even with accurate concept representations, explanations may not provide precise localizations. This discrepancy may occur when a model’s perception of a concept differs from human expectation. For instance, in the case of the microscope-artifact, all models captured only the border of the circle rather than the entire area. Consequently, if the model’s understanding of a concept does not align with human expectations, the explanation may be ineffective for bias localization.
- *Bias Mitigation:* With imperfect bias representations, bias mitigation approaches may cause collateral damage, *i.e.*, unlearning of valid concepts entangled with biased concepts. This can be overcome with improved concept disentanglement.

Moreover, bias mitigation methods, especially post-hoc model editing, might not sufficiently foster valid behavior, but only unlearn invalid strategies. Although successfully unlearning the targeted bias, this can lead to poor model performance on clean data.

8 Conclusions

In this work, we introduce an XAI-based framework for the identification of spurious shortcut behavior in DNNs from both data and model perspective. We utilize concept-based bias representations for the semi-automated computation of sample- and pixel level bias annotations. Our work is integrated into the Reveal2Revise framework, providing valuable insights for bias mitigation and re-evaluation. We successfully demonstrated the applicability of the framework by identifying and mitigation spurious correlations caused by controlled and real-world data artifacts in four medical datasets across two modalities, using VGG16, ResNet50, and ViT model architectures. Future work may explore the identification and mitigation of biases in disentangled concept spaces, *e.g.*, leveraging SAEs. Another promising direction is the integration of expected concepts for a more targeted search for unexpected concepts.

Acknowledgements We thank Melina Zeeb for assistance with visualizations. This work was supported by the Federal Ministry of Education and Research (BMBF) as grant BIFOLD (01IS18025A, 01IS180371I); the German Research Foundation (DFG) as research unit DeSBI (KI-FOR 5363 – project ID: 459422098); the European Union’s Horizon Europe research and innovation programme (EU Horizon Europe) as grant TEMA (101093003); the European Union’s Horizon 2020 research and innovation programme (EU Horizon 2020) as grant iToBoS (965221).

References

- [1] Reduan Achtibat, Maximilian Dreyer, Ilona Eisenbraun, Sebastian Bosse, Thomas Wiegand, Wojciech Samek, and Sebastian Lapuschkin. From attribution maps to human-understandable explanations through concept relevance propagation. *Nat Mach Intell*, 5(9):1006–1019, 2023.
- [2] Guillaume Alain and Yoshua Bengio. Understanding intermediate layers using linear classifier probes. *ICLR*, 2017.
- [3] Christopher J Anders, Leander Weber, David Neumann, Wojciech Samek, Klaus-Robert Müller, and Sebastian Lapuschkin. Finding and removing clever hans: Using explanation methods to debug and improve deep models. *Information Fusion*, 77:261–295, 2022.
- [4] Sebastian Bach, Alexander Binder, Grégoire Montavon, Frederick Klauschen, Klaus-Robert Müller, and Wojciech Samek. On pixel-wise explanations for non-linear classifier decisions by layer-wise relevance propagation. *PloS one*, 10(7):e0130140, 2015.
- [5] Dilyara Bareeva, Maximilian Dreyer, Frederik Pahde, Wojciech Samek, and Sebastian Lapuschkin. Reactive model correction: Mitigating harm to task-relevant features via conditional bias suppression. In *CVPRW*, pages 3532–3541, 2024.
- [6] David Bau, Jun-Yan Zhu, Hendrik Strobelt, Agata Lapedriza, Bolei Zhou, and Antonio Torralba. Understanding the role of individual units in a deep neural network. *Proceedings of the National Academy of Sciences*, 117(48):30071–30078, 2020.
- [7] Yonatan Belinkov. Probing classifiers: Promises, shortcomings, and advances. *Computational Linguistics*, 48(1):207–219, 2022.
- [8] Nora Belrose, David Schneider-Joseph, Shauli Ravfogel, Ryan Cotterell, Edward Raff, and Stella Biderman. Leace: Perfect linear concept erasure in closed form. *NeurIPS*, 36, 2024.
- [9] Alceu Bissoto, Eduardo Valle, and Sandra Avila. Debiasing skin lesion datasets and models? not so fast. In *CVPRW*, pages 740–741, 2020.
- [10] Hanna Borgli, Vajira Thambawita, Pia H Smedsrud, Steven Hicks, Debesh Jha, Sigrun L Eskeland, Kristin Ranheim Randel, et al. Hyperkvasir, a comprehensive multi-class image and video dataset for gastrointestinal endoscopy. *Scientific data*, 7(1):283, 2020.
- [11] Judy Borowski, Roland Simon Zimmermann, Judith Schepers, Robert Geirhos, Thomas SA Wallis, Matthias Bethge, and Wieland Brendel. Natural images are more informative for interpreting cnn activations than state-of-the-art synthetic feature visualizations. In *NeurIPS 2020 Workshop SVRHM*, 2020.
- [12] Markus M Breunig, Hans-Peter Kriegel, Raymond T Ng, and Jörg Sander. Lof: identifying density-based local outliers. In *Proceedings of the 2000 ACM SIGMOD*, pages 93–104, 2000.
- [13] Trenton Bricken, Adly Templeton, Joshua Batson, Brian Chen, Adam Jermyn, Tom Conerly, Nick Turner, Cem Anil, Carson Denison, et al. Towards monosemanticity: Decomposing language models with dictionary learning. *Transformer Circuits Thread*, 2, 2023.
- [14] Titus J Brinker, Achim Hekler, Alexander H Enk, Joachim Klode, Axel Hauschild, Carola Berking, Bastian Schilling, Sebastian Haferkamp, Dirk Schadendorf, et al. Deep learning outperformed 136 of 157 dermatologists in a head-to-head dermoscopic melanoma image classification task. *European Journal of Cancer*, 113:47–54, 2019.
- [15] Alexander Brown, Nenad Tomasev, Jan Freyberg, Yuan Liu, Alan Karthikesalingam, and Jessica Schrouff. Detecting shortcut learning for fair medical ai using shortcut testing. *Nature communications*, 14(1):4314, 2023.
- [16] Kirill Bykov, Mayukh Deb, Dennis Grinwald, Klaus-Robert Müller, and Marina MC Höhne.

- Dora: Exploring outlier representations in deep neural networks. In *ICLR Workshops*, 2023.
- [17] Kirill Bykov, Laura Kopf, Shinichi Nakajima, Marius Kloft, and Marina Höhne. Labeling neural representations with inverse recognition. *NeurIPS*, 36, 2024.
- [18] Bill Cassidy, Connah Kendrick, Andrzej Brodzicki, Joanna Jaworek-Korjakowska, and Moi Hoon Yap. Analysis of the isic image datasets: Usage, benchmarks and recommendations. *Medical image analysis*, 75:102305, 2022.
- [19] Noel CF Codella, David Gutman, M Emre Celebi, Brian Helba, Michael A Marchetti, Stephen W Dusza, Aadi Kalloo, et al. Skin lesion analysis toward melanoma detection: A challenge at the 2017 international symposium on biomedical imaging (isbi), hosted by the international skin imaging collaboration (isic). In *15th International Symposium on Biomedical Imaging (ISBI 2018)*, pages 168–172. IEEE, 2018.
- [20] Marc Combalia, Noel CF Codella, Veronica Rotemberg, Brian Helba, Veronica Vilaplana, Ofer Reiter, Cristina Carrera, et al. Bcn20000: Dermoscopic lesions in the wild, 2019.
- [21] Jonathan Crabbé and Mihaela van der Schaar. Concept activation regions: A generalized framework for concept-based explanations. *NeurIPS*, 35:2590–2607, 2022.
- [22] Antonio De Santis, Riccardo Campi, Matteo Bianchi, and Marco Brambilla. Visual-tcav: Concept-based attribution and saliency maps for post-hoc explainability in image classification. *arXiv preprint arXiv:2411.05698*, 2024.
- [23] Alex J DeGrave, Joseph D Janizek, and Su-In Lee. Ai for radiographic covid-19 detection selects shortcuts over signal. *Nat Mach Intell*, 3(7):610–619, 2021.
- [24] Jia Deng, Wei Dong, Richard Socher, Li-Jia Li, Kai Li, and Li Fei-Fei. Imagenet: A large-scale hierarchical image database. In *CVPR*, pages 248–255. IEEE, 2009.
- [25] Misha Denil, Babak Shakibi, Laurent Dinh, Marc’Aurelio Ranzato, and Nando De Freitas. Predicting parameters in deep learning. *NeurIPS*, 26, 2013.
- [26] Alexey Dosovitskiy, Lucas Beyer, Alexander Kolesnikov, Dirk Weissenborn, et al. An image is worth 16x16 words: Transformers for image recognition at scale. *ICLR*, 2021.
- [27] Maximilian Dreyer, Reduan Achtibat, Wojciech Samek, and Sebastian Lapuschkin. Understanding the (extra-) ordinary: Validating deep model decisions with prototypical concept-based explanations. In *CVPRW*, pages 3491–3501, 2024.
- [28] Maximilian Dreyer, Frederik Pahde, Christopher J Anders, Wojciech Samek, and Sebastian Lapuschkin. From hope to safety: Unlearning biases of deep models via gradient penalization in latent space. In *AAAI*, volume 38, pages 21046–21054, 2024.
- [29] Maximilian Dreyer, Erblina Purlku, Johanna Vielhaben, Wojciech Samek, and Sebastian Lapuschkin. Pure: Turning polysemantic neurons into pure features by identifying relevant circuits. In *CVPRW*, pages 8212–8217, 2024.
- [30] Maximilian Dreyer, Jim Berend, Tobias Labarta, Johanna Vielhaben, Thomas Wiegand, Sebastian Lapuschkin, and Wojciech Samek. Mechanistic understanding and validation of large ai models with semanticlens. *arXiv preprint arXiv:2501.05398*, 2025.
- [31] Nelson Elhage, Tristan Hume, Catherine Olson, Nicholas Schiefer, Tom Henighan, Shauna Kravec, et al. Toy models of superposition. *arXiv preprint arXiv:2209.10652*, 2022.
- [32] Logan Engstrom, Andrew Ilyas, Shibani Santurkar, Dimitris Tsipras, Brandon Tran, and Aleksander Madry. Adversarial robustness as a prior for learned representations. *arXiv preprint arXiv:1906.00945*, 2019.
- [33] Dumitru Erhan, Yoshua Bengio, Aaron Courville, and Pascal Vincent. Visualizing higher-layer features of a deep network. *University of Montreal*, 1341(3):1, 2009.
- [34] Thomas Fel, Agustin Picard, Louis Bethune, Thibaut Boissin, David Vigouroux, Julien Colin, Rémi Cadène, and Thomas Serre. Craft: Concept recursive activation factorization for explainability. In *CVPR*, pages 2711–2721, 2023.
- [35] Thomas Fel, Thibaut Boissin, Victor Boutin, Agustin Picard, Paul Novello, Julien Colin, Drew Linsley, Tom Rousseau, Remi Cadene,

- Lore Goetschalckx, et al. Unlocking feature visualization for deep network with magnitude constrained optimization. *NeurIPS*, 36, 2024.
- [36] Thomas Fel, Victor Boutin, Louis Béthune, Rémi Cadène, Mazda Moayeri, Léo Andéol, Mathieu Chalvidal, and Thomas Serre. A holistic approach to unifying automatic concept extraction and concept importance estimation. *NeurIPS*, 36, 2024.
- [37] Ronald A Fisher. The use of multiple measurements in taxonomic problems. *Annals of eugenics*, 7(2):179–188, 1936.
- [38] Ruth Fong and Andrea Vedaldi. Net2vec: Quantifying and explaining how concepts are encoded by filters in deep neural networks. In *CVPR*, pages 8730–8738, 2018.
- [39] Robert Geirhos, Jörn-Henrik Jacobsen, Claudio Michaelis, Richard Zemel, Wieland Brendel, et al. Shortcut learning in deep neural networks. *Nat Mach Intell*, 2(11):665–673, 2020.
- [40] Amirata Ghorbani, James Wexler, James Y Zou, and Been Kim. Towards automatic concept-based explanations. *NeurIPS*, 32, 2019.
- [41] Mara Graziani, An-phi Nguyen, Laura O’Mahony, Henning Müller, and Vincent Andrearczyk. Concept discovery and dataset exploration with singular value decomposition. In *ICLR Workshops*, 2023.
- [42] Kaiming He, Xiangyu Zhang, Shaoqing Ren, and Jian Sun. Deep residual learning for image recognition. In *CVPR*, pages 770–778, 2016.
- [43] Tong He, Zhi Zhang, Hang Zhang, Zhongyue Zhang, Junyuan Xie, and Mu Li. Bag of tricks for image classification with convolutional neural networks. In *CVPR*, pages 558–567, 2019.
- [44] Evan Hernandez, Sarah Schwettmann, David Bau, Teona Bagashvili, Antonio Torralba, and Jacob Andreas. Natural language descriptions of deep visual features. In *ICLR*, 2021.
- [45] Robert Huben, Hoagy Cunningham, Logan Riggs Smith, Aidan Ewart, and Lee Sharkey. Sparse autoencoders find highly interpretable features in language models. In *ICLR*, 2023.
- [46] Jeremy Irvin, Pranav Rajpurkar, Michael Ko, Yifan Yu, et al. Chexpert: A large chest radiograph dataset with uncertainty labels and expert comparison. In *AAAI*, 2019.
- [47] Been Kim, Martin Wattenberg, Justin Gilmer, Carrie Cai, James Wexler, Fernanda Viegas, et al. Interpretability beyond feature attribution: Quantitative testing with concept activation vectors (tcav). In *ICML*, pages 2668–2677. PMLR, 2018.
- [48] Sebastian Lapuschkin, Stephan Wäldchen, Alexander Binder, Grégoire Montavon, Wojciech Samek, and Klaus-Robert Müller. Unmasking clever hans predictors and assessing what machines really learn. *Nature Communications*, 10(1):1096, 2019.
- [49] Leland McInnes, John Healy, Nathaniel Saul, and Lukas Großberger. Umap: Uniform manifold approximation and projection. *Journal of Open Source Software*, 3(29), 2018.
- [50] Georgii Mikriukov, Gesina Schwalbe, Christian Hellert, and Korinna Bade. Evaluating the stability of semantic concept representations in cnns for robust explainability. In *World Conference on Explainable Artificial Intelligence*, pages 499–524. Springer, 2023.
- [51] Niels JS Morch, Ulrik Kjems, Lars Kai Hansen, Claus Svarer, Ian Law, Benny Lautrup, Steve Strother, and Kelly Rehm. Visualization of neural networks using saliency maps. In *ICNN*, volume 4, pages 2085–2090. IEEE, 1995.
- [52] W James Murdoch, Peter J Liu, and Bin Yu. Beyond word importance: Contextual decomposition to extract interactions from lstms. *ICLR*, 2018.
- [53] Yannic Neuhaus, Maximilian Augustin, Valentin Boreiko, and Matthias Hein. Spurious features everywhere-large-scale detection of harmful spurious features in imagenet. In *ICCV*, 2023.
- [54] Tuomas Oikarinen and Tsui-Wei Weng. Clip-dissect: Automatic description of neuron representations in deep vision networks. In *ICLR*, 2023.
- [55] Chris Olah, Alexander Mordvintsev, and Ludwig Schubert. Feature visualization. *Distill*, 2(11):e7, 2017.
- [56] Chris Olah, Nick Cammarata, Ludwig Schubert, Gabriel Goh, Michael Petrov, and Shan Carter. Zoom in: An introduction to circuits. *Distill*, 5(3):e00024–001, 2020.
- [57] Nobuyuki Otsu et al. A threshold selection method from gray-level histograms. *Automatica*, 11(285-296):23–27, 1975.

- [58] Frederik Pahde, Maximilian Dreyer, Leander Weber, Moritz Weckbecker, Christopher J Anders, Thomas Wiegand, Wojciech Samek, and Sebastian Lapuschkin. Navigating neural space: Revisiting concept activation vectors to overcome directional divergence. *arXiv preprint arXiv:2202.03482*, 2022.
- [59] Frederik Pahde, Maximilian Dreyer, Wojciech Samek, and Sebastian Lapuschkin. Reveal to revise: An explainable ai life cycle for iterative bias correction of deep models. In *MICCAI*, 2023.
- [60] Adam Paszke, Sam Gross, Francisco Massa, Adam Lerer, James Bradbury, et al. Pytorch: An imperative style, high-performance deep learning library. *NeurIPS*, 32, 2019.
- [61] Alec Radford, Rafal Jozefowicz, and Ilya Sutskever. Learning to generate reviews and discovering sentiment. *arXiv preprint arXiv:1704.01444*, 2017.
- [62] Laura Rieger, Chandan Singh, William Murdoch, and Bin Yu. Interpretations are useful: penalizing explanations to align neural networks with prior knowledge. In *ICML*, 2020.
- [63] Andrew Slavin Ross, Michael C Hughes, and Finale Doshi-Velez. Right for the right reasons: training differentiable models by constraining their explanations. In *IJCAI*, 2017.
- [64] Ramprasaath R Selvaraju, Michael Cogswell, Abhishek Das, Ramakrishna Vedantam, Devi Parikh, and Dhruv Batra. Grad-cam: Visual explanations from deep networks via gradient-based localization. In *ICCV*, pages 618–626, 2017.
- [65] Karen Simonyan and Andrew Zisserman. Very deep convolutional networks for large-scale image recognition. In Yoshua Bengio and Yann LeCun, editors, *ICLR 2015*, 2015.
- [66] S Singla and S Feizi. Salient imagenet: How to discover spurious features in deep learning. In *ICLR*, 2022.
- [67] Djordje Slijepcevic, Fabian Horst, Sebastian Lapuschkin, Brian Horsak, Anna-Maria Raberger, Andreas Kranzl, Wojciech Samek, Christian Breiteneder, Wolfgang Immanuel Schöllhorn, and Matthias Zeppelzauer. Explaining machine learning models for clinical gait analysis. *ACM Transactions on Computing for Healthcare (HEALTH)*, 3(2):1–27, 2021.
- [68] Nils Strodthoff, Patrick Wagner, Tobias Schaeffter, and Wojciech Samek. Deep learning for ecg analysis: Benchmarks and insights from ptb-xl. *IEEE journal of biomedical and health informatics*, 25(5):1519–1528, 2020.
- [69] Christian Szegedy, Wojciech Zaremba, Ilya Sutskever, Joan Bruna, Dumitru Erhan, Ian Goodfellow, and Rob Fergus. Intriguing properties of neural networks. In *ICLR*, 2014.
- [70] Philipp Tschandl, Cliff Rosendahl, and Harald Kittler. The ham10000 dataset, a large collection of multi-source dermatoscopic images of common pigmented skin lesions. *Scientific data*, 5(1):1–9, 2018.
- [71] Laurens Van der Maaten and Geoffrey Hinton. Visualizing data using t-sne. *JMLR*, 9(11), 2008.
- [72] Johanna Vielhaben, Stefan Bluecher, and Nils Strodthoff. Multi-dimensional concept discovery (mcd): A unifying framework with completeness guarantees. *TMLR*, 2023.
- [73] Patrick Wagner, Nils Strodthoff, Ralf-Dieter Boussejot, Dieter Kreiseler, Fatima I Lunze, Wojciech Samek, and Tobias Schaeffter. Ptb-xl, a large publicly available electrocardiography dataset. *Scientific data*, 7(1):1–15, 2020.
- [74] Patrick Wagner, Temesgen Mehari, Wilhelm Haverkamp, and Nils Strodthoff. Explaining deep learning for ecg analysis: Building blocks for auditing and knowledge discovery. *Computers in Biology and Medicine*, 176:108525, 2024.
- [75] Nina Weng, Paraskevas Pegios, Eike Petersen, Aasa Feragen, and Siavash Bigdeli. Fast diffusion-based counterfactuals for shortcut removal and generation. In *ECCV*, 2025.
- [76] Ross Wightman. Pytorch image models. <https://github.com/rwightman/pytorch-image-models>, 2019.
- [77] Shirley Wu, Mert Yuksekogun, Linjun Zhang, and James Zou. Discover and cure: Concept-aware mitigation of spurious correlation. In *ICML*, 2023.
- [78] John R Zech, Marcus A Badgeley, Manway Liu, Anthony B Costa, Joseph J Titano, and Eric Karl Oermann. Variable generalization performance of a deep learning model to detect pneumonia in chest radiographs: a cross-sectional study. *PLoS medicine*, 15(11), 2018.

- [79] Ruihan Zhang, Prashan Madumal, Tim Miller, Krista A Ehinger, and Benjamin IP Rubinstein. Invertible concept-based explanations for cnn models with non-negative concept activation vectors. In *AAAI*, volume 35, pages 11682–11690, 2021.
- [80] Bolei Zhou, Aditya Khosla, Agata Lapedriza, Aude Oliva, and Antonio Torralba. Learning deep features for discriminative localization. In *CVPR*, pages 2921–2929, 2016.

A Appendix

In the following, we will provide additional details and mathematical foundations for CAV-based bias modeling approaches in Sec. A.1, biased sample retrieval in Sec. A.2, and bias mitigation approaches in Sec. A.3. We will then provide experimental details regarding the datasets in Sec. A.4 and model training in Sec. A.5. This is followed by additional experimental results in Sec. A.6, including XAI-driven shortcut identification for both ECG and vision data (Sec. A.6.1), biased sample retrieval (Sec. A.6.2), spatial bias localization (Sec. A.6.3), and bias mitigation (Sec. A.6.4).

A.1 Bias Modeling

In this work, we model biases either via individual neurons or directions in latent space, *i.e.*, CAVs. Traditionally, a CAV is computed by fitting a linear classifier separating samples *with* the concept to be modeled from samples *without* the concept. The weight vector, *i.e.*, the vector perpendicular to the decision hyperplane, is considered as the concept direction. However, CAVs obtained as weights from linear classifiers can be susceptible to distractor signals in the data and therefore fail in precisely estimating the concept *signal* direction. To tackle this, Pattern-CAVs have been proposed as an alternative [58]. Whereas CAVs obtained from SVM weights are superior in predicting the presence of a concept (*e.g.*, for biased sample retrieval), Pattern-CAVs are more suitable to precisely model the concept direction (*e.g.*, for CLArC-based bias mitigation). In the following, we provide the mathematical foundation for both approaches.

SVM-CAV The most common choice for CAVs are weight vectors from SVMs. Specifically, SVMs [82] find a hyperplane maximizing the margin between two classes using the hinge loss, defined as $l_i = \max(0, 1 - t_i (\mathbf{h}^\top \mathbf{x}_i + b))$ and L_2 -norm regularization with the following optimization objective:

$$\mathbf{h}^{\text{SVM}}, b = \operatorname{argmin}_{\mathbf{h}, b} \left\{ \frac{1}{n} \sum_{i \in [n]} l_i + \lambda \sqrt{\sum_{j \in [m]} w_j^2} \right\}. \quad (4)$$

Pattern-CAV Pattern-CAVs [58] can be computed based on the covariance between the latent activations $\mathbf{a}(\mathbf{x})$ and the concept labels t as:

$$\mathbf{h}_l^{\text{pat}} = \frac{1}{\sigma_t^2 |\mathcal{X}|} \sum_{\mathbf{x}, t \in \mathcal{X}} (\mathbf{a}_l(\mathbf{x}) - \bar{\mathcal{A}}_l)(t - \bar{t}) \quad (5)$$

with mean latent activation $\bar{\mathcal{A}}$, mean concept label \bar{t} and sample concept label variance σ_t^2 , which is equal to the sample covariance between the latent activations $\mathbf{a}(\mathbf{x})$ and the concept labels t divided by the sample concept label variance.

A.2 Biased Sample Retrieval

Inspired by the idea behind RelMax, the identification of biased samples can also be implemented using relevance scores, as an alternative to the activation-based biased sample retrieval described in Eq. 1 in the main paper. Specifically, we can compute a bias score $\mathbf{s}_{\text{bias}}^{\text{rel}}$ by projecting the *relevance* for the prediction of a sample \mathbf{x} onto the concept direction $\mathbf{h}\mathbf{r}_l^c$, computed similar as CAVs, but using latent relevances scores, instead of activations, on layer l w.r.t. class c :

$$\mathbf{s}_{\text{bias}}^{\text{rel}} = \mathbf{h}\mathbf{r}_l^c \top \mathbf{r}_l^c(\mathbf{x}) \quad (6)$$

with latent relevances $\mathbf{r}_l^c(\mathbf{x})$ w.r.t. class c computed on layer l by a local attribution method, *e.g.*, using LRP. As the relevance is computed in a class-specific manner, this approach further allows distinguishing concepts that are artifactual for certain classes but valid features for others.

A.3 Bias Mitigation

A.3.1 Regularization-based Bias Mitigation

Recent approaches define a loss function designed to encourage or enforce pre-defined behavior. Therefore, additional prior information \mathbf{A} encoding *expected* behavior is required. This leads to an overall loss $\mathcal{L}_{\text{total}}$ based on a λ -weighted sum of the classification loss $\mathcal{L}_{\text{class}}$ and the newly constructed “right-reason” loss term \mathcal{L}_{RR} :

$$\mathcal{L}_{\text{total}}(\mathbf{x}, \mathbf{y}, \mathbf{A}) = \mathcal{L}_{\text{class}}(\mathbf{x}, \mathbf{y}) + \lambda \mathcal{L}_{\text{RR}}(\mathbf{x}, \mathbf{A}). \quad (7)$$

Input (heatmap-based) Bias mitigation approaches on input level require sample-wise pixel-level annotations, indicating the presence of a data artifact, available as prior knowledge. This prior information can be used to align expected behavior with the model’s prediction strategy. Specifically, RRR [63] introduces a loss term penalizing the alignment between the input gradient, *i.e.*, the gradient of the prediction w.r.t. the input, and (binary) input masks localizing the data artifact. Hence, the model is penalized for paying attention on undesired regions. Given an input sample \mathbf{x} along with bias localization

mask \mathbf{m} , the loss for RRR is defined as

$$\mathcal{L}_{\text{RR}}^{\text{input}}(\mathbf{x}, \mathbf{m}) = (\nabla_{\mathbf{x}} \log(f_{\theta}(\mathbf{x})) \circ \mathbf{m})^2. \quad (8)$$

Alternatively, Rieger et al. [62] propose Contextual Decomposition Explanation Penalization (CDEP), using Contextual Decomposition importance scores [52] importance scores [52] instead of the gradient to encode model behavior to be aligned with prior knowledge.

Note, however, that pixel-wise annotations for expected model behavior are expensive to obtain, leading to practical limitations. Concept localization approaches, as described in Sec. 3.3, can be utilized to semi-automate this process. Another limitation of input-level bias mitigation approaches is their inability to address spatially distributed and interconnected biases. Spurious correlations that are spread over the entire image, such as color shifts or overlapping other important concepts, cannot be effectively mitigated at the input level.

Latent space (CAV-based) To overcome aforementioned limitations, recent work introduces the ClArC framework [3] that leverages latent concept representations using CAVs for bias mitigation which has two advantages. First, using the latent space alleviates the reliance on spatial locations and therefore allows the correction of unlocalized biases, such as color shifts. Moreover, the annotation costs are substantially lower, since only sample-level concept labels are required for the computation of CAVs, instead of pixel-level artifact masks. Given the bias representation in the form of a CAV, the ClArC framework unlearns related model behavior by either adding or removing activations in the artifact direction. Built upon this idea, Dreyer et al. [28] introduce RR-ClArC, utilizing a loss function inspired by RRR which penalizes the feature use measured through the *latent* gradient pointing into the direction of the bias, as modeled via the CAV. More precisely, given a bias direction \mathbf{h} , the latent right reason loss $\mathcal{L}_{\text{RR}}^{\text{latent}}$ is defined as

$$\mathcal{L}_{\text{RR}}^{\text{latent}}(\mathbf{x}, \mathbf{h}) = (\nabla_{\mathbf{a}} \tilde{f}(\mathbf{a}(\mathbf{x})) \cdot \mathbf{h})^2. \quad (9)$$

Intuitively, this loss term penalizes the model if it changes the prediction behavior when activations in the bias direction are added/subtracted, corresponding to the addition/removal of the modeled artifact. Note, that the latent gradient is computed w.r.t. a chosen class, allowing for class-specific bias mitigation.

A.3.2 Post-hoc Model Editing

To further reduce the computational requirements for bias mitigation, another line of works removes undesired behavior by post-hoc model editing in training-free manner. This group of bias mitigation approaches commonly models the undesired concept as a linear direction in latent space, followed by a modification of latent representations or model parameters to make model predictions invariant towards the modeled direction. As such, P-ClArC [3] utilizes CAVs to model the concept to be erased and projects out activations into the concept direction during inference time. Specifically, given CAV \mathbf{h}_l and latent activations $\mathbf{a}_l(\mathbf{x})$ for layer l , the activations are overwritten to $\mathbf{a}'_l(\mathbf{x})$ as

$$\mathbf{a}'_l(\mathbf{x}) = \mathbf{a}_l(\mathbf{x}) - \lambda(\mathbf{x})\mathbf{h}_l \quad (10)$$

with perturbation strength $\lambda(\mathbf{x})$ based on the input sample \mathbf{x} , for instance chosen such that activations in CAV direction are equal to the average value of clean (non-artifactual) samples. Intuitively, subtracting activations along the concept direction in latent space is equivalent to removing the concept in input space. The modification can be performed either for all samples [3] or in a reactive manner [5], conditioned for example on the predicted class label or the existence of the spurious feature.

Similarly, SpuFix [53] models concepts as PCA components in the activation space in layer l and overwrites activations for spurious directions by $\min(\alpha_k^c, 0)$, with α_k^c being the activations for the spurious PCA component k for class c , thereby not allowing positive contributions in the spurious direction. Ravfogel et al. [85] perform an iterative null-space projection of linear directions encoding the undesired concept to make sure the concept cannot be recovered from other directions. Santurkar et al. [86] suggest classifier editing, a procedure modifying the model weights directly to shift the model’s prediction behavior. Most recently, LEast-squares Concept Erasure (LEACE) [8] is a closed-form solution for concept erasure, minimally changing the model’s internal representations on *all* layers. It is to note, however, that post-hoc editing approaches can lead to “collateral damage”, meaning that whereas the concept is successfully suppressed for biased samples, the model modification can have a negative impact on clean samples, as further discussed by Bareeva et al. [5].

A.4 Dataset Details

We run experiments for the datasets ISIC2019 for image-based melanoma detection, HyperKvasir for

the identification of abnormal conditions in the gastrointestinal track, CheXpert with chest radiographs, and PTB-XL for the prediction of cardiovascular diseases from ECG data. ISIC2019 consists of 25,331 samples classified into eight lesion types, both malignant and benign. The HyperKvasir dataset contains 10,662 samples labeled into 23 classes of findings. We aggregate the findings into two classes representing findings with and without disease to consider the task as a binary classification task. The CheXpert dataset is a collection of 224,316 chest radiographs of 65,240 patients with labels for 14 conditions, including cardiomegaly. We solve a binary classification task by predicting the presence of cardiomegaly. We use a subset of 28,878 samples with additional annotations for the presence of pacemakers provided by Weng et al. [75]. Lastly, in addition to vision data, we use the PTB-XL dataset containing 21,837 records of 10 second 12-lead ECG data (time series data) and labels for 23 cardiovascular conditions. We report details for all considered datasets in Tab. 2. Specifically, we report the number of classes and samples, train/validation/test-splits and considered data artifacts. We use ISIC2018 for multi-class classification and consider the real-world artifacts **ruler**, **skin-marker**, and **reflection**, as well as the artificial **brightness** artifact inserted into 20% of samples of class “melanoma”. For **ruler** (all classes) and **band-aid** (only occurring in “melanocytic nevus”), we use labels indicating the existence of the artifact provided by Anders et al. [3]. For HyperKvasir, we split the classes into “normal”/“no-disease” and “abnormal”/“disease” to implement the task as a binary classification task, as described in Tab. 3. We insert a **timestamp** artifact into 10% of the the training samples with label “disease”, and, in addition, consider the real-world artifact **insertion tube**. The latter was primarily detected in samples from class “no disease”. For CheXpert, we solve a binary classification task to predict the presence of the class “cardiomegaly”. We limit our experiments to a subset of the CheXpert dataset for which Weng et al. [75] provide labels for the existence of the naturally occurring **pacemaker** artifact (mainly in class “cardiomegaly”). In addition, we artificially increase the **brightness** in 10% of “cardiomegaly” samples as a controlled artifact. Lastly, we use the PTB-XL dataset with ECG-data for multi-class classification into cardiovascular conditions. As a controlled artifact, we insert a **static noise** (constant high value) into the first second of one lead (II-lead) for 50% of samples of class “left ventricular hypertrophy”.

A.5 Training Details

We provide training details for all considered models in Tab. 4. This includes VGG16, ResNet50 and ViT model architecture for vision datasets, *i.e.*, ISIC2019, HyperKvasir, and CheXpert, each both with and without controlled artifact. We use model checkpoints from the PyTorch model zoo (`torchvision`) [60] for VGG16 (weights: `VGG16_Weights.IMAGENET1K_V1`) and ViT-B-16 (weights: `ViT_B_16_Weights.IMAGENET1K_V1`) models, as well as from `timm` [76], specifically the checkpoint named `resnet50d.a3_in1k` for ResNet50. Moreover, we train a XResNet1d50 model for the (controlled) PTB-XL dataset. We report accuracy and false positive rate (FPR) for the affected class on a clean and, for controlled settings, an attacked test set, with artifacts inserted into *all* samples. We train models with an initial learning rate $\alpha \in \{0.005, 0.001, 0.005\}$, either with SGD or Adam optimizers. We divide the learning rate by 10 after 150 and 250 epochs, respectively, for vision datasets (50/75 for PTB-XL), and select α and the optimizer for the final model based on the performance on the validation set. Note, that a large gap between accuracy and FPR on the *clean* compared to the *attacked* test set indicates that the model is sensitive towards the artifact, *i.e.*, it picks up the spurious correlation.

A.6 Additional Results

This section will provide additional experimental results. Specifically, we report results for the XAI-driven shortcut identification for both ECG and vision data in Sec. A.6.1, the biased sample retrieval in Sec. A.6.2, the spatial bias localization in Sec. A.6.3, and, lastly, bias mitigation in Sec. A.6.4.

A.6.1 Detection of Spurious Model Behavior

In the following, we apply the considered spurious behavior detection approaches, from both data and model perspective, to all datasets, including ECG and vision data.

ECG Data (XResNet1d50) First, we apply SpRAy (data perspective) and pairwise cosine similarities between max-pooled relevance scores (model perspective) to the ECG data in PTB-XL with the controlled **static noise** artifact in Fig. 10. Whereas the application of SpRAy reveals a coherent cluster of poisoned samples, they do not appear as *outlier*, but instead as *inlier* behavior. This indicates that the prediction behavior is very dominant, potentially due to the high poisoning rate of 50%. However, the

Table 2: Details for considered datasets, including ISIC2019, HyperKvasir, CheXpert, and PTB-XL. We report the number of classes and samples, the train/val/test-splits, and the considered data artifacts. For the latter, we further report whether the artifact is controlled (or real-world) and, if applicable, in which class it occurs. For controlled artifacts, we further report the percentage of samples of the attacked class in which the artifact is inserted.

name	classes	samples	train/val/test	artifact	controlled	artifact class (%)
ISIC2019	8	25,331	0.8/0.1/0.1	microscope	yes	melanoma (20%)
				ruler	no	-
				band-aid	no	melanocytic nevus
				skin marker	no	-
				reflection	no	mainly benign keratosis
HyperKvasir	2	10,662	0.8/0.1/0.1	timestamp	yes	disease (10%)
				insertion tube	no	mainly no disease
CheXpert	2	28,878	0.8/0.1/0.1	brightness	yes	cardiomegaly (10%)
				pacemaker	no	mainly cardiomegaly
PTB-XL	23	21,837	0.8/0.1/0.1	static noise (II-lead)	yes	left ventricular hypertrophy (50%)

Table 3: Categorization of classes in HyperKvasir into “disease” and “no-disease”.

class	sub-classes
disease	“barretts”, “short-segment-barretts”, “oesophagitis-a”, “oesophagitis-b-d”, “hemorrhoids”, “hemorrhoids”, “polyp”, “ulcerative-colitis-grade-0-1”, “ulcerative-colitis-grade-1-2”, “ulcerative-colitis-grade-2-3”, “ulcerative-colitis-grade-1”, “ulcerative-colitis-grade-2”, “ulcerative-colitis-grade-3”, “dyed-lifted-polyps”, “impacted-stool”
no-disease	“bbps-0-1”, “bbps-2-3”, “dyed-resection-margins”, “ileum”, “retroflex-rectum”, “retroflex-stomach”, “normal-cecum”, “normal-pylorus”, “normal-z-line”

model perspective reveals an outlier cluster of concepts clearly focusing on the inserted artifact (see neurons #125 and #180). Moreover, we apply PCX, which further allows the analysis of inlier behavior by revealing prediction sub-strategies for considered classes, as shown in Fig. 11. We can clearly identify **prototype 1** as sub-strategy using the inserted **static noise** artifact, with high relevance scores for the related concepts detected by neuron #125 and #180. Note, that the prototype covers 50% of the test data, which is exactly the inserted poisoning rate.

Vision Data (VGG16 and ResNet50) In Fig. 12, we apply bias detection approaches from the data perspective (*left*) and model perspective (*right*) to the VGG16 model trained on HyperKvasir using relevance scores for neurons on the last (13th) conv layer. We detect a coherent, but not outlier

cluster with samples containing the **insertion tube** from the data perspective, as well as a set of concepts focusing on the artifact from the model perspective. The application of PCX, however, reveals a sub-strategy for class “non-disease” with prototypical samples all containing the artifact, as shown in Fig. 21 (*left*).

Next, we apply our bias detection approaches to the ResNet50 model trained on HyperKvasir with the controlled **timestamp** artifact using relevance scores after the 3rd residual block for samples from the attacked class (“disease”) in Fig.13. SpRAy reveals a clear outlier cluster of poisoned samples containing the artifact (*left*) and the concept clustering reveals a coherent set of concepts focusing on the inserted **timestamp** (*right*, see neurons #60, #499, and #910). We further apply PCX in Fig. 21 (*right*), clearly revealing **prototype 0** with related concepts

Table 4: Model performance and training details for all considered datasets and architectures. We train VGG16, ResNet50, and ViT models for vision datasets, *i.e.*, ISIC2019, HyperKvasir, and CheXpert, in the original and controlled version, respectively. Moreover, we train an XResNet1d50 model for ECG data in PTB-XL. We report the accuracy and false positive rate (FPR) on a clean and, for controlled datasets, an attacked test set. The FPR is computed w.r.t. the attacked class in the controlled settings, and for classes “melanoma” (ISIC2019), “Disease” (HyperKvasir) and “cardiomegaly” (CheXpert) for the original datasets. In addition, we report training details including optimizer, learning rate (LR) and number of training epochs. The former two are selected based on the performance on the validation set.

Dataset	Model	Accuracy \uparrow		FPR \downarrow		Training details		
		clean	attacked	clean	attacked	Optim.	LR	epochs
ISIC2019	VGG16	0.82	-	0.09	-	SGD	0.001	300
	ResNet50	0.88	-	0.03	-	Adam	0.0005	300
	ViT	0.79	-	0.05	-	SGD	0.005	300
ISIC2019 (attacked)	VGG16	0.85	0.25	0.04	0.88	SGD	0.001	300
	ResNet50	0.87	0.28	0.02	0.85	Adam	0.001	300
	ViT	0.81	0.27	0.04	0.85	SGD	0.005	300
Hyper- Kvasir	VGG16	0.96	-	0.02	-	SGD	0.001	300
	ResNet50	0.97	-	0.01	-	Adam	0.0005	300
	ViT	0.95	-	0.02	-	SGD	0.005	300
Hyper- Kvasir (attacked)	VGG16	0.97	0.68	0.02	0.39	SGD	0.005	300
	ResNet50	0.97	0.60	0.02	0.48	Adam	0.001	300
	ViT	0.93	0.42	0.01	0.70	SGD	0.001	300
CheXpert	VGG16	0.83	-	0.08	-	SGD	0.001	300
	ResNet50	0.82	-	0.08	-	Adam	0.001	300
	ViT	0.80	-	0.09	-	SGD	0.005	300
CheXpert (attacked)	VGG16	0.83	0.52	0.07	0.58	SGD	0.005	300
	ResNet50	0.81	0.42	0.09	0.73	Adam	0.005	300
	ViT	0.80	0.25	0.12	0.97	SGD	0.0005	300
PTB-XL (attacked)	XResNet1d50	0.96	0.94	0.00	0.43	Adam	0.001	100

#499 and #910 as prediction sub-strategy focusing on the inserted `timestamp` artifact.

For CheXpert, in Fig. 14 we reveal an outlier cluster of samples containing the `pacemaker` artifact from the data perspective (*left*), and concepts focusing on the artifact from the model perspective (*right*) using relevances for neurons on the 10th conv layer. The application of PCX for samples of the class “cardiomegaly” does not clearly reveal an impacted prototype, as shown in Fig. 22 (*left*). However, all prototypes have high relevance scores for neuron #436, which appears to focus on artifacts such as the considered `pacemaker`.

Moreover, we run bias identification approaches for CheXpert with the controlled `brightness` artifact inserted into class “cardiomegaly” using relevance scores for neurons on the 12th conv layer of

the VGG16 model in Fig. 15. Whereas the data perspective reveals a clear outlier cluster of affected samples (*left*), no outlier concepts can be detected and the interpretation of considered samples w.r.t. the `brightness` artifact is challenging (*right*). Note, that we selected concepts revealed via PCX in Fig. 22 (*right*), with `prototype 3` appearing to focus on samples containing the `brightness` artifact with high relevance scores for neurons #89 and #143.

For ISIC2019 with the controlled `microscope` artifact, we show bias identification results using relevance scores after the 3rd residual block of the ResNet50 model in Fig. 16. The data perspective (*left*) reveals an outlier cluster of samples focusing on the inserted artifact (\bullet), and, interestingly, also a cluster focusing on a different type of black circles (\bullet). The model perspective (*right*) reveals a large outlier

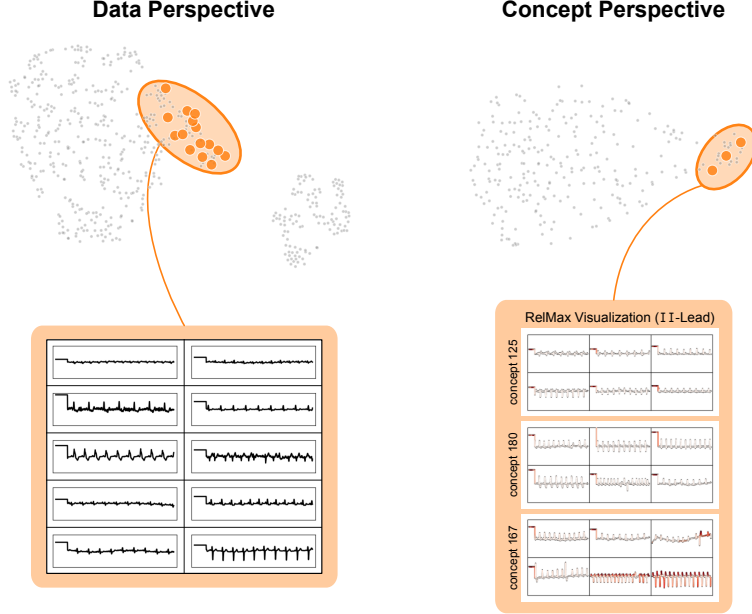


Figure 10: Artifact identification on the last conv layer of a XResNet50 model trained on ECG data from the PTB-XL dataset with samples from the “LVH”-class using SpRAy on latent relevances for the data perspective (*left*) and pair-wise cosine similarities for the model perspective (*right*). For the data perspective, we identify a coherence set of samples containing the inserted `static noise` artifact in the poisoned lead. However, as the controlled artifact is very dominant, the prediction behavior manifests as *inlier*, not as *outlier*. From the model perspective, we identify a set of outlier concepts focusing on the artifact in the II-lead.

set of concepts focusing on the black border caused by the `microscope` artifact. Similarly, the application of PCX in Fig. 23 (*left*) leads to `prototype 2` as shown in Fig. 20. Interestingly, the application of PCX as sub-strategy for the attacked class, clearly using the inserted artifact with high relevance scores for neurons #910 and #499.

To reveal real-world artifacts in ISIC2019, we apply shortcut identification approaches using relevance scores after the 3rd residual block of the ResNet50 model using samples from classes “melanoma”, “melanocytic nevus”, and “benign keratosis”, respectively. The application of SpRAy reveals the usage of the `ruler` artifact for the prediction of “melanoma” (see Fig. 17, *left*), the `band-aid` artifact for the prediction of the benign class “melanocytic nevus” (see Fig. 17, *right*), as well as the usage of the artifacts `reflection` (●) and `skin marker` (●) for class “benign keratosis” (Fig. 18). From the model perspective, we can reveal the usage of outlier neurons focusing on the concepts `blueish tint` (●) and `ruler` (●) for class “melanoma”, as shown in Fig. 19 (*left*). For the class “benign keratosis”, the model uses outlier neurons focusing on the concepts `reflection` (●) and `ruler` (●), as shown in Fig. 19 (*right*). Lastly, the concept perspective reveals neurons for several con-

founders for the class “melanocytic nevus”, including `band-aids` (●), `rulers` (●), and `white hair/lines` (●), as shown in Fig. 20. Interestingly, the application of PCX on samples from class “melanocytic nevus” using relevances after the 4th residual block in Fig. 23 (*right*) reveals `prototype 0`, which is a sub-strategy relying on the concept `red skin` and related neurons #1147 and #1737.

Vision Data (ViT) The interpretation of neurons on the last layer of ViTs poses a particular challenge, as they are not preceded by a ReLU non-linearity. As such, both positive and negative activations are possible and the amplitude of the activations cannot be interpreted as the degree of existence of a certain concept. However, we apply bias identification approaches from the data perspective (SpRAy), model perspective (pairwise cosine similarities between neurons) and the combination thereof (PCX) on relevance scores for the `class-token` on the last layer. Fig. 24 shows that the data perspective (*left*) can clearly reveal samples with the `brightness` artifact in CheXpert, but the model perspective (*right*) does not detect outlier concepts focussing on the artifact. We highlight concepts revealed via the application of

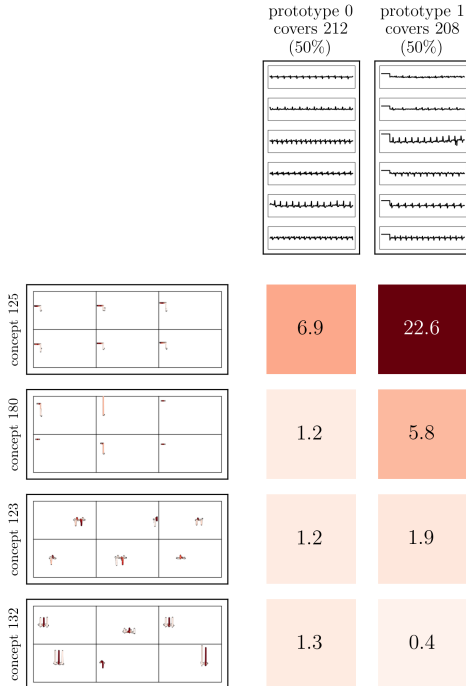


Figure 11: PCX visualizations using latent relevances after the last residual block of the XResNet50 model trained on PTB-XL with the controlled **static noise** artifact. Only samples from the attacked class “LVH” are considered. Columns represent prototypes with the signal coming from the attacked lead of six representative samples, rows represent concepts (visualized via RelMax) and the values in the matrix indicate the average relevance of the concept for the prototype. **Prototype 1** clearly focuses on the inserted **static noise** artifact, with high scores for the related concepts (neurons) #125 and #180.

PCX in Fig. 25 (*left*), leading to **prototype 3** with a clear focus on the artifact on high average relevance scores for concepts #371, #279 and #99. For HyperKvasir, PCX does not reveal a prototype mainly focusing on the **brightness**, but instead prototypes that distinguish by clinically valid features (Fig. 25, *right*).

A.6.2 Biased Sample Retrieval

In addition to our experiments in Sec. 6.3, we report quantitative biased sample retrieval results via AUROC and AP for the real-world artifacts **band-aid**, **ruler** (both ISIC2019) and **pacemaker** (CheXpert), as well as for the controlled artifacts **microscope** (ISIC2019), **timestamp** (HyperKvasir), and **brightness** (CheXpert) in Tabs. 5 and 6 for CAV-based and individual-neuron-based bias scores, respectively. For the latter, the best performing neuron is selected on the validation set and results are reported for an unseen test set. We further show the distribution of CAV-based bias scores for clean and biased samples for the artifacts **band-aid**

and **skin marker** (both ISIC2019) in Fig. 26, for the controlled artifacts **microscope** (ISIC2019) and **timestamp** (HyperKvasir) in Fig. 27, and lastly for **brightness** (CheXpert) in Fig. 28. The following models and layers are used for the distribution plots: last Conv layer of ResNet50 for **band-aid**, 11th Conv layer of VGG16 for **skin marker** in ISIC2019, 3rd residual block of ResNet50 for **microscope** for the controlled ISIC2019 dataset, 10th Conv layer of VGG16 for **timestamp** in the controlled HyperKvasir dataset, as well as the 3rd residual block of ResNet50 and the last linear layer of ViT for the controlled **brightness** artifact in CheXpert.

A.6.3 Spatial Bias Localization

Complementing our experiments in Sec. 6.4, we report our quantitative bias localization results, specifically the artifact relevance and IoU, for the controlled artifacts **microscope** (ISIC2019) and **timestamp** (HyperKvasir) in tabular form in Tab. 7. Moreover, we show exemplary concept heatmaps and binary localization masks using CAVs on the best performing

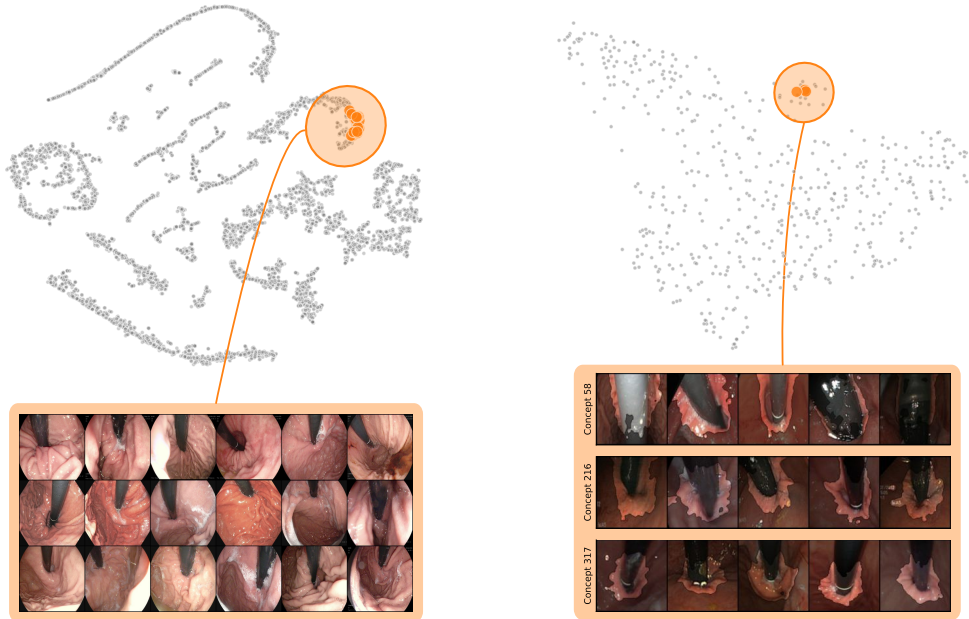


Figure 12: Artifact identification on the last (13th) conv layer of a VGG16 model trained on HyperKvasir with samples from the “no-disease”-class using SpRAy on latent relevances for the data perspective (*left*) and pair-wise cosine similarities for the model perspective (*right*). While not being a clear outlier, there is a coherent set of samples (data perspective) and concepts (model perspective) focussing on the **insertion tube** artifact.

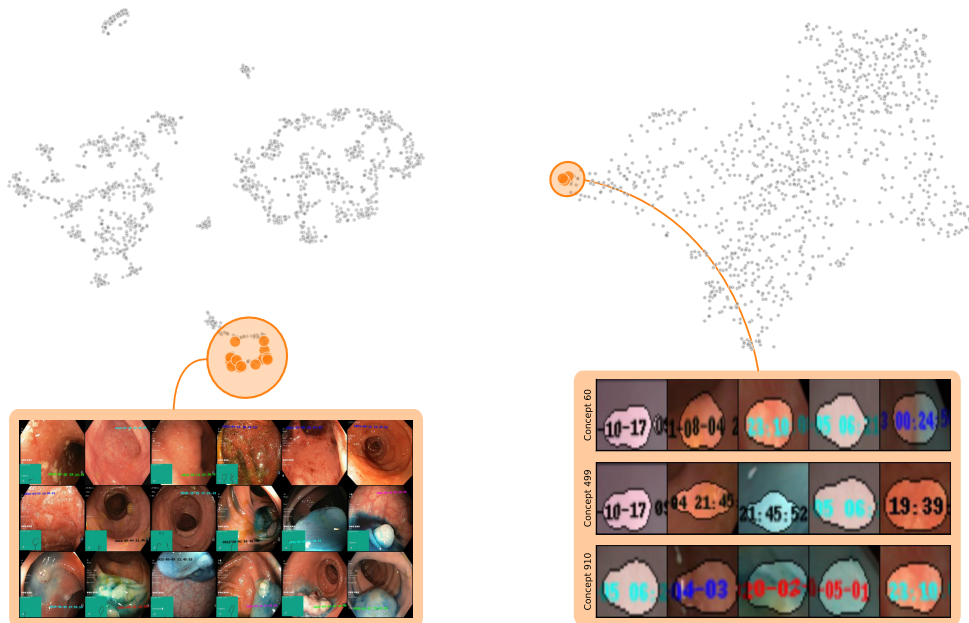


Figure 13: Bias identification after the 3rd residual block of a ResNet50 model trained on HyperKvasir using the controlled **timestamp** artifact with samples from the “disease”-class using SpRAy on latent relevances for the data perspective (*left*) and pair-wise cosine similarities for the model perspective (*right*). We identify a clear outlier cluster with biased samples (data perspective) and a coherent set of concepts focusing on the considered artifact (model perspective).

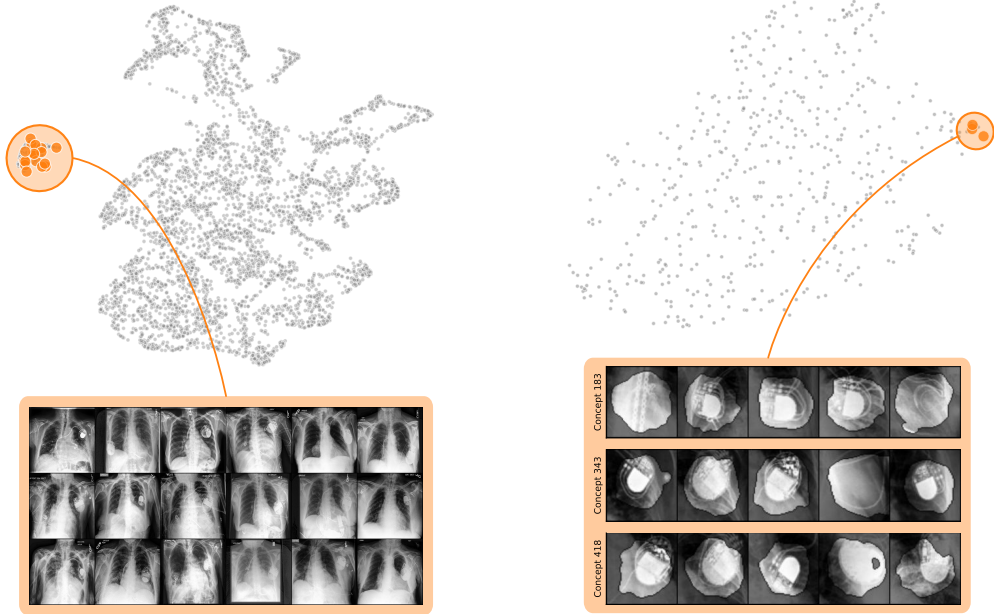


Figure 14: Bias identification after the 10th conv layer of a VGG16 model trained on CheXpert with samples from the “cardiomegaly”-class using SpRAy on latent relevances for the data perspective (*left*) and pair-wise cosine similarities for the model perspective (*right*). We identify a clear outlier cluster with samples containing the **pacemaker** artifact (*left*) and an outlier set of concepts focusing on the artifact (*right*).

layer of VGG16 and ResNet50 in Figs. 29 and 30 for **microscope** and **timestamp**, respectively. For the **microscope** artifact, both models only detect the border of the circle instead of the entire area. This leads to low IoU scores, as the metric also measures what the computed mask does *not* cover.

In addition, we show computed localizations for real-world artifacts **band-aid**, **ruler** (both ISIC2019), **pacemaker** (CheXpert), and **insertion tube** (HyperKvasir) in Figs. 31 and 32. These localizations can be valuable inputs to bias mitigation approaches, such as RRR, as well as for the computation of metrics measuring the artifact reliance, *e.g.*, the artifact relevance. We further show artifact localizations for the controlled artifacts **microscope** (ISIC2019) and **timestamp** (HyperKvasir) using ViT models in Fig. 33. Due to the lack of reliable solutions for backpropagation-based local explanation methods for ViT architectures, we apply SHapley Additive exPlanations (SHAP) [83] on superpixels computed via simple linear iterative clustering (SLIC) [81] to explain the output of the CAV to compute concept heatmaps. Note, that this approach highly limits the flexibility of the bias localization due to the pre-defined image structure given by the pixel statistics forming superpixels.

A.6.4 Bias Mitigation

In the following, we provide additional bias mitigation results with our controlled artifacts, namely the **static noise** in ECG data (PTB-XL), the **timestamp** (HyperKvasir), and **microscope** (ISIC2019). Specifically, we compare the accuracy on a clean test set and a biased test set, where the artifact is artificially inserted into samples from all classes. Moreover, we measure the model’s sensitivity towards the bias concept by computing (1) the percentage of relevance, measured via LRP and (2) the TCAV score [47]. The latter is based on the concept sensitivity measured via CAV \mathbf{h} and the latent feature use, computed as gradient of the prediction w.r.t. latent activations $\mathbf{a}(\mathbf{x})$:

$$\text{TCAV}_{\text{sens}}(\mathbf{x}) = \nabla_{\mathbf{a}} \tilde{f}(\mathbf{a}(\mathbf{x})) \cdot \mathbf{h} . \quad (11)$$

Given a subset containing the bias concept $\mathcal{X}_b = \{\mathbf{x}_i \in \mathcal{X} \mid t_i = 1\}$, the TCAV score is measured as the percentage of samples with positive sensitivity towards changes along the estimated concept direction \mathbf{h} and is computed as

$$\text{TCAV} = \frac{|\{\mathbf{x} \in \mathcal{X}_b \mid \text{TCAV}_{\text{sens}}(\mathbf{x}) > 0\}|}{|\mathcal{X}_b|} . \quad (12)$$

Hence, a TCAV score of 0.5 indicates no concept

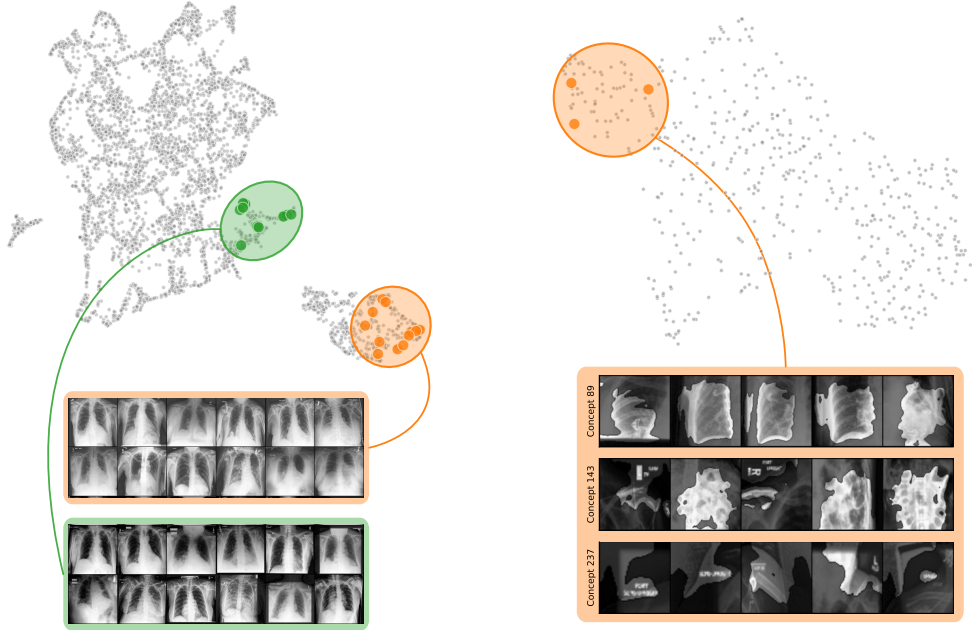


Figure 15: Bias identification after the 12th conv layer of a VGG16 model trained on CheXpert using the controlled **brightness** artifact with samples from the “cardiomegaly”-class using SpRAY on latent relevances for the data perspective (*left*) and pair-wise cosine similarities for the model perspective (*right*). We identify a clear outlier cluster with samples with the **brightness** artifact (●, *left*). For comparison, we further highlight a cluster of samples with clean samples (●). Note, that it is challenging to identify the artifact from the model perspective, as related concept visualizations do not reveal the **brightness**. Since there is no outlier concept, we visualize concepts that are highly relevant for the prediction sub-strategy revealed via PCX (see Fig. 22).

reliance, while higher or lower scores are interpreted as negative and positive influence, respectively. We report $\Delta\text{TCAV} = |\text{TCAV} - 0.5|$, where 0 indicates no sensitivity and higher values are interpreted as reliance on the artifact.

In Tab. 8, we report results for PTB-XL, using the bias mitigation methods RRR, RR-ClArC, and P-ClArC, in comparison with a Vanilla model without a bias-aware loss term. All bias mitigation approaches, particularly ClArC-based methods, successfully increase the accuracy and decrease the false positive rate (for the attacked class LVH) on the biased test set. RR-ClArC and P-ClArC successfully reduce the artifact relevance, but have little impact on the TCAV score. For the former, instead of using a spatial mask localizing the artifact, we use temporal masks and compute the percentage of relevance put onto the attacked time span, *i.e.*, the first second.

Additional results for the vision datasets with controlled artifacts (HyperKvasir - **timestamp** | ISIC2019 - **microscope** | CheXpert - **brightness**) are shown in Tabs. 9 and 10 for VGG16 and ResNet50 model architectures, respectively. For the correction method

RRR, in addition to the mitigation results using ground truth masks (gt), we include results for model correction with automatically computed artifacts masks using relevance heatmaps (hm) and binarized masks using Otsu’s method (bin). For VGG16, RRR outperforms other mitigation approaches for the correction of the easily localizable **timestamp** artifact in HyperKvasir. For ISIC2019 (see Tab. 9), whereas P-ClArC outperforms other approaches in terms of artifact relevance and ΔTCAV , it has a poor performance in terms of accuracy on the biased test set. This can be explained by the fact that post-hoc model-editing does not allow the model to learn alternative prediction strategies when biases are unlearned. For CheXpert, RR-ClArC achieves the best results for biased accuracy and ΔTCAV . Note, that we refrained from reporting results for RRR on CheXpert, as we consider the **brightness** artifact as unlocalizable in input space. Interestingly, the application of P-ClArC leads to a drastic decrease in accuracy on the clean dataset, which can be explained by collateral damage [5], *i.e.*, the suppression of related, yet relevant concept directions. For ResNet50 (see

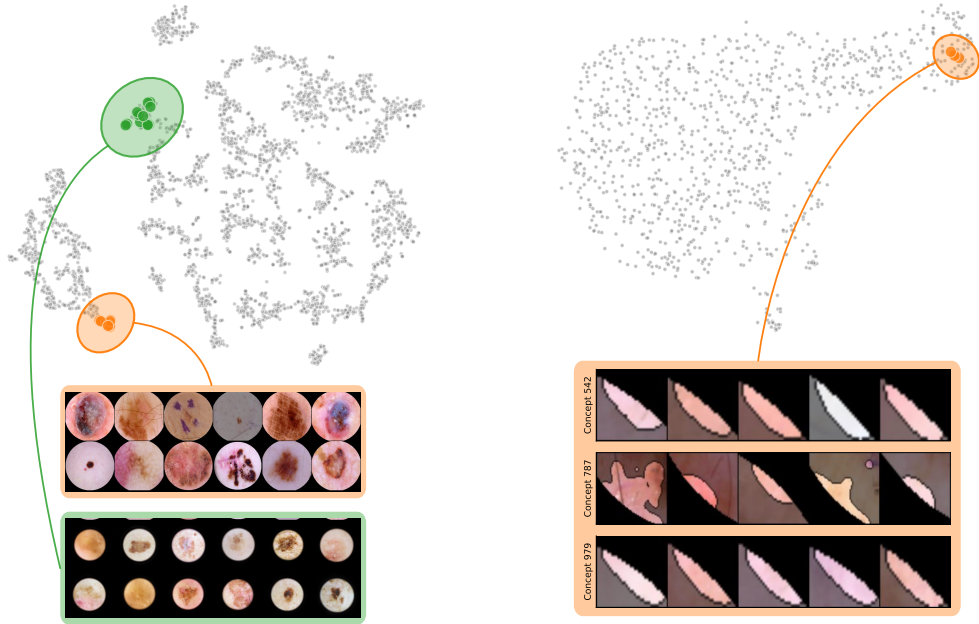


Figure 16: Bias identification after the 3rd residual block of a ResNet50 model trained on ISIC2019 using the controlled `microscope` artifact with samples from the “melanoma”-class using SpRAY on latent relevances for the data perspective (*left*) and pair-wise cosine similarities for the model perspective (*right*). We identify multiple clusters with samples with different versions of the `microscope` artifact (*left*) and a large outlier set of concepts focusing on the black circle (*right*).

Tab. 10), RR-ClArC outperforms other bias mitigation approaches across all considered datasets and metrics, and achieves accuracies on the biased test sets that are close to those on the clean test sets. Lastly, in Tab. 11 we report bias mitigation results for ViT models. Note that instead of reporting ΔTCAV , we report $\text{TCAV}_{\text{sens}}$ results directly to obtain more fine-grained results. Especially RRR is capable of mitigating the considered biases to some extent in terms of biased accuracy and artifact relevance and RR-ClArC performs best in terms of $\text{TCAV}_{\text{sens}}$.

Qualitative Bias Mitigation Results In addition to the quantitative bias mitigation results discussed in Sec. A.6.4, we show qualitative findings in Fig. 34. Specifically, we show local explanations as relevance heatmaps computed with LRP for models corrected via RRR in comparison with the Vanilla model for VGG16 models trained on the controlled versions of the ISIC2019 and HyperKvasir datasets. We selected test samples from the attacked classes, *i.e.*, “melanoma” for ISIC2019 containing the `microscope` artifact and “disease” from HyperKvasir with the artificial `timestamp`. Whereas the Vanilla models focus on the artifacts, the corrected models shift their attention to medically relevant features.

This trend is confirmed by the quantitative results in Tab. 9, with decreased artifact relevance for RRR (gt) runs in comparison with the Vanilla model.

Hyperparameters Bias mitigation approaches utilizing a bias-aware loss term, such as RRR and RR-ClArC, require a hyperparameter λ , balancing between the classification loss and the auxiliary loss term, as defined in Eq. 7. High values can lead to collateral damage by “over-correcting” the targeted bias and low values might have no impact. Therefore, we test values $\lambda \in \{1^1, 5 \cdot 1^1, 1^2, 5 \cdot 1^2, \dots, 5 \cdot 1^9\}$ for RRR, and $\lambda \in \{1^1, 5 \cdot 1^1, 1^2, 5 \cdot 1^2, \dots, 5 \cdot 1^{12}\}$ for RR-ClArC. We pick the best performing λ values on the validation set and report the bias mitigation results on an unseen test set. The selected λ values are shown in Tab. 12. As learning rate, we use the learning rate used during training (see Tab. 4) divided by 10.

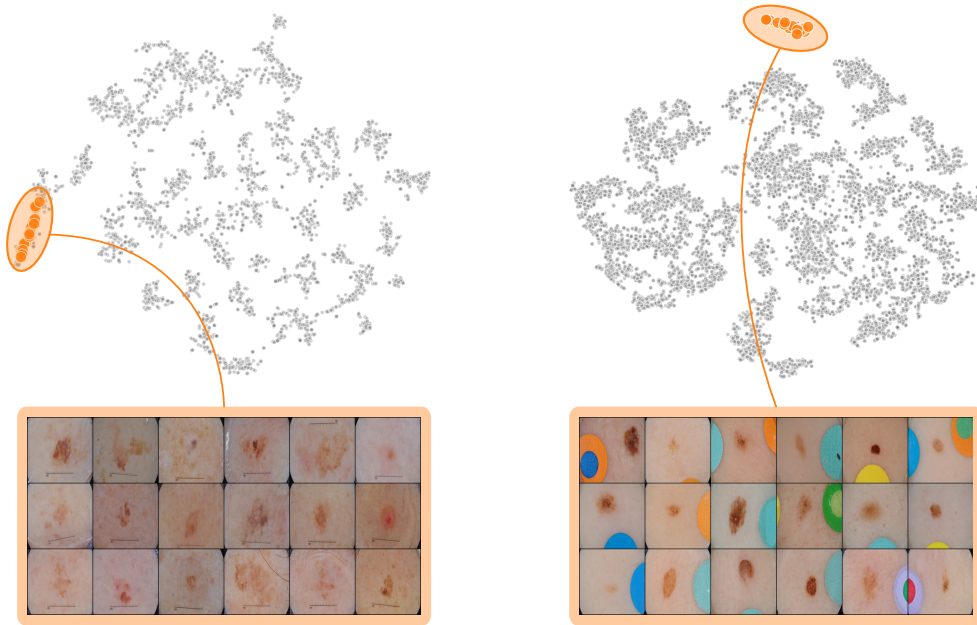


Figure 17: Bias identification from the data perspective using SpRAy with relevances after the 3rd residual block of a ResNet50 model trained on ISIC2019 using samples from classes “melanoma” (*left*) and “melanocytic nevus” (*right*). We identify clear outlier clusters with samples containing the **ruler** (*left*, “melanoma”) and **band-aid** (*right*, “melanocytic nevus”) artifacts.

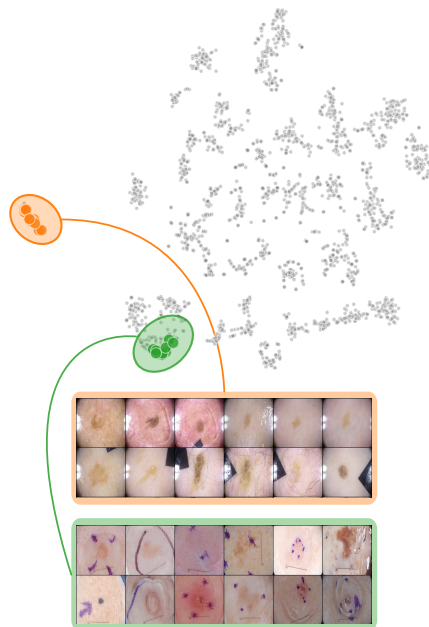


Figure 18: Bias identification from the data perspective using SpRAy with relevances after the 3rd residual block of a ResNet50 for ISIC2019 using samples from the class “benign keratosis”. We identify outlier clusters with samples containing the **reflection** (●) and **skin marker** (●) artifacts.

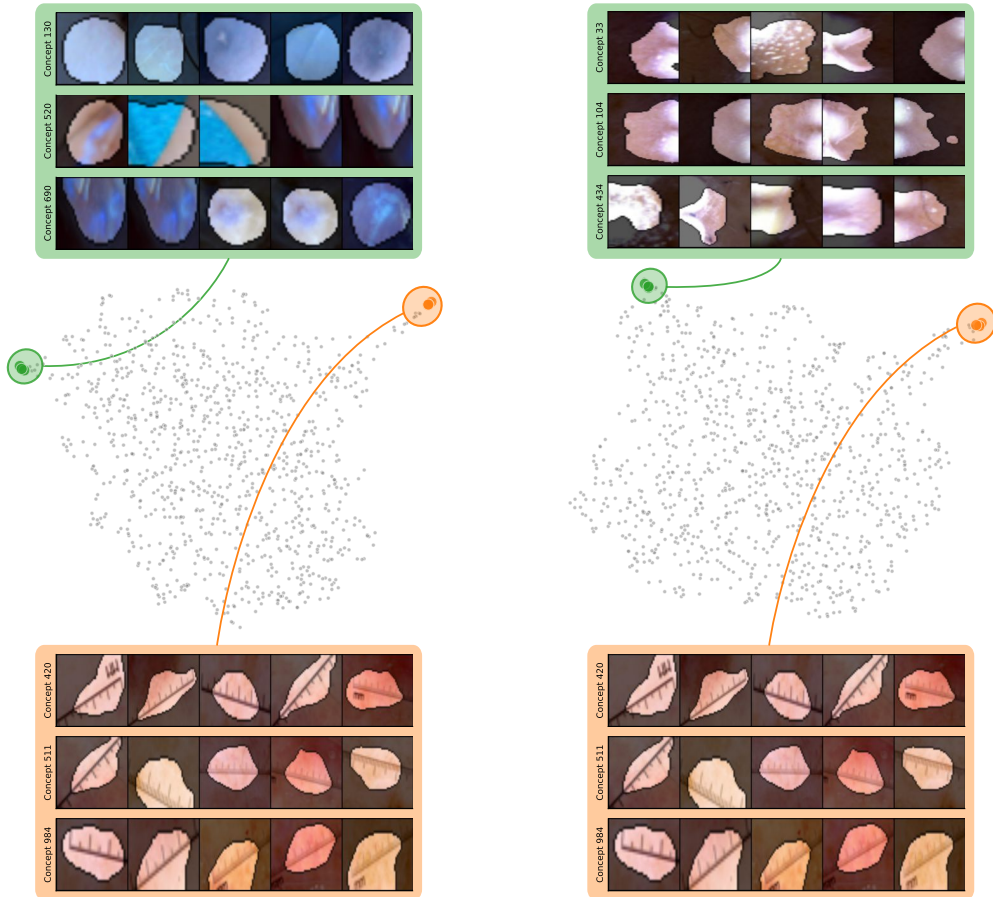


Figure 19: Bias identification from the model perspective using pair-wise cosine similarities between max-pooled relevances after the 3rd residual block of a ResNet50 for ISIC2019 using samples from the classes “melanoma” (*left*) and “benign keratosis” (*right*). For “melanoma”, we identify outlier concepts focusing on the ruler (●) and blueish tint (●) artifacts. For “benign keratosis”, We identify outlier concepts focussing on reflections (●), and, again rulers (●). For the latter, predictions for both considered classes use exactly the same neurons.

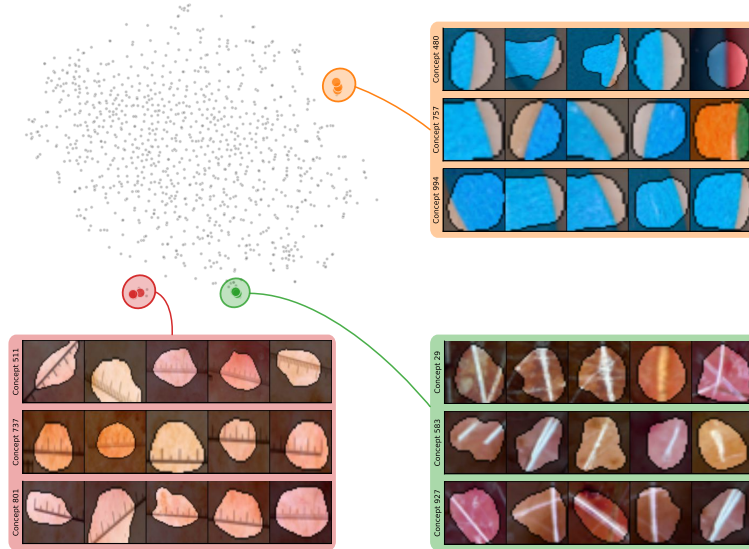


Figure 20: Bias identification from the model perspective using pair-wise cosine similarities between max-pooled relevances after the 3rd residual block of a ResNet50 for ISIC2019 using samples from the class “melanocytic nevus”. We identify outlier concepts focusing on the ruler (●), white hair/lines (●), and band-aid (●) artifacts.

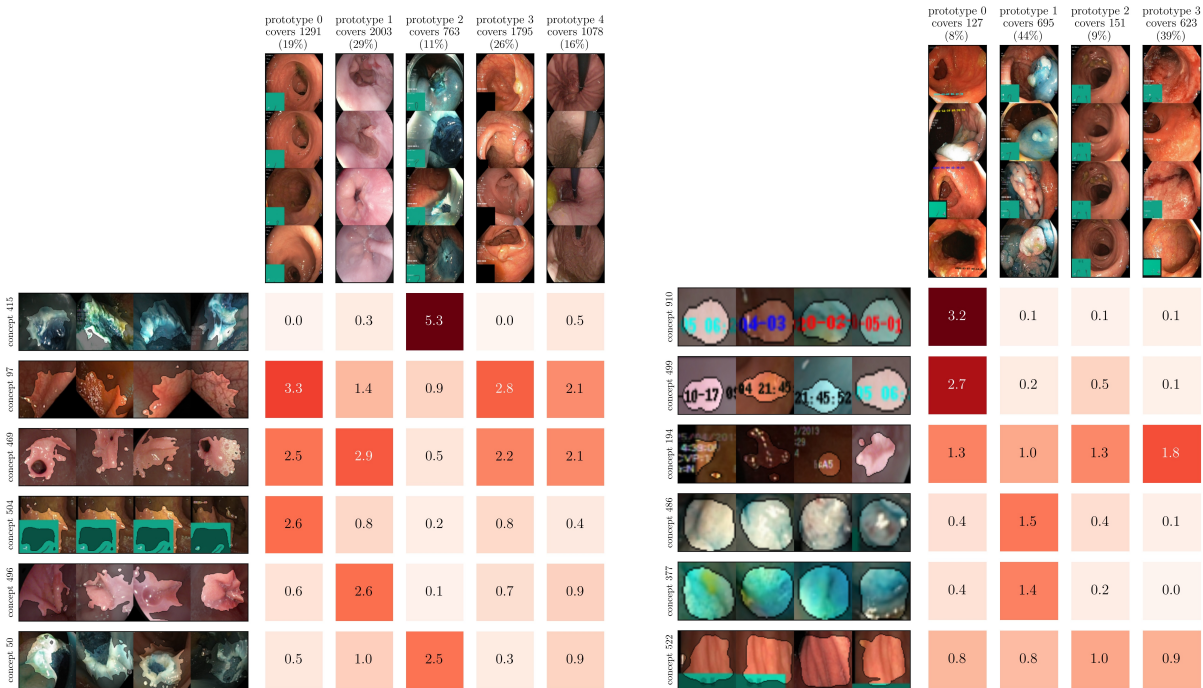


Figure 21: PCX visualizations using latent relevances after the last (13th) conv layer of a VGG16 model trained on HyperKvasir (*left*) and after the 3rd residual block of a ResNet50 model trained on HyperKvasir with the controlled `timestamp` artifact (*right*). Only samples from the class “no disease” are considered. Columns represent prototypes with four representative samples, rows represent concepts (visualized via RelMax) and the values in the matrix indicate the average relevance of the concept for the prototype. For clean HyperKvasir (*left*), prototype 4 focuses on the insertion tubes. However, no artifact-related concept is associated with the prototype. For the controlled HyperKvasir experiment (*right*), prototype 0 focuses on the `timestamp` artifact with high scores for the related concepts #910 and #499.

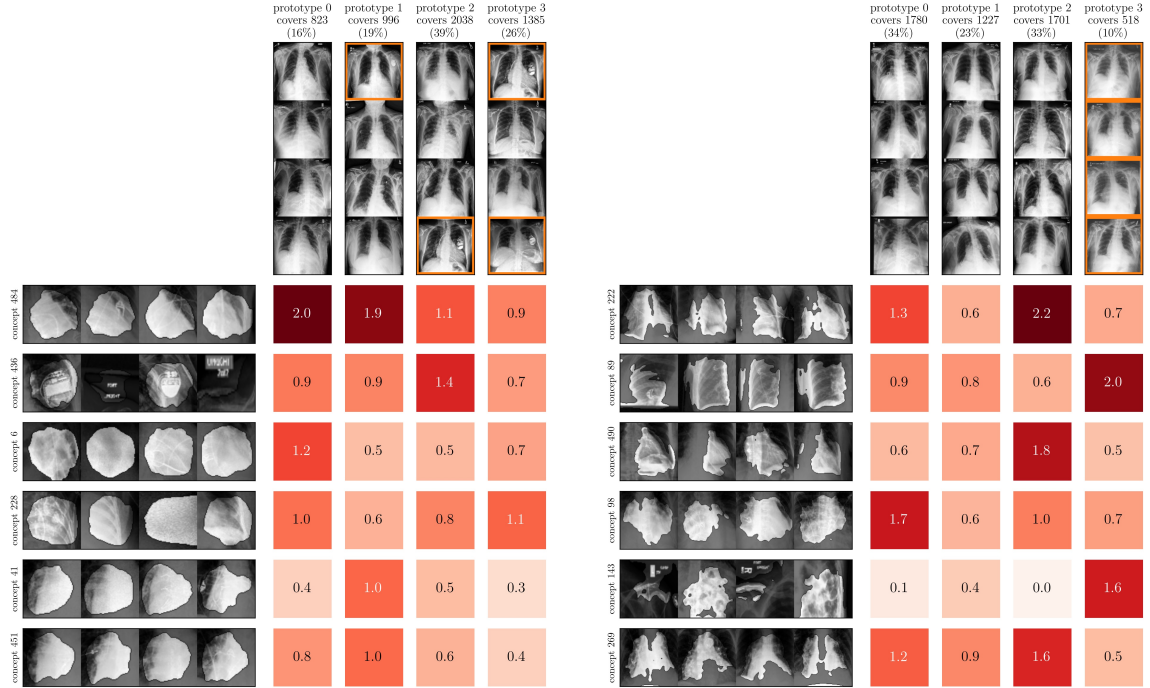


Figure 22: PCX visualizations using latent relevances after the 12th and 10th conv layers of VGG16 models trained on the original CheXpert data (*left*) and with controlled **brightness** artifact (*right*). Only samples from the class “cardiomegaly” are considered. Columns represent prototypes with four representative samples, rows represent concepts (visualized via RelMax) and the values in the matrix indicate the average relevance of the concept for the prototype. To ease readability, prototypical samples containing the expected artifacts **pacemaker** (*right*) and **brightness** (*left*) are highlighted with an orange box. For **pacemaker** (*left*), the artifact appears in multiple prototypes, but concept #436, relevant to most prototypes, appears to focus on the artifact. For the controlled **brightness** artifact (*right*), **prototype 3** focuses on the considered artifact with high scores for the hard-to-interpret concepts (neurons) #89 and #143.

Table 5: Quantitative results for CAV-based biased sample retrieval w.r.t. the real-world artifacts **band-aid**, **ruler** (both ISIC2019), and **pacemaker** (CheXpert), as well as the controlled artifacts **microscope** (ISIC2019), **timestamp** (HyperKvasir), and **brightness** (CheXpert). We report AUROC and AP to evaluate the ranking capabilities of CAV-based bias scores using activations on different layers of VGG16, ResNet50, and ViT models. Higher scores are better.

	layer	ISIC2019						HypKvasir		CheXpert			
		band-aid		ruler		microscope		timestamp		pacemaker		brightness	
		AUC	AP	AUC	AP	AUC	AP	AUC	AP	AUC	AP	AUC	AP
VGG16	Conv 4	1.0	0.99	0.99	0.85	0.98	0.89	0.97	0.85	0.70	0.16	1.0	0.97
	Conv 7	1.0	1.00	1.00	0.92	0.97	0.86	0.93	0.63	0.91	0.62	1.0	0.98
	Conv 10	1.0	1.00	1.00	0.93	0.98	0.86	0.98	0.74	0.98	0.87	1.0	1.00
	Conv 13	1.0	0.98	1.00	0.88	0.96	0.84	0.98	0.43	0.96	0.82	1.0	1.00
ResNet50	Block 1	1.0	1.0	1.0	0.87	0.99	0.92	0.98	0.87	0.76	0.26	1.0	1.0
	Block 2	1.0	1.0	1.0	0.90	0.99	0.91	0.99	0.87	0.95	0.75	1.0	1.0
	Block 3	1.0	1.0	1.0	0.92	0.98	0.86	1.00	0.96	0.97	0.83	1.0	1.0
	Block 4	1.0	1.0	1.0	0.88	0.99	0.91	1.00	0.94	0.95	0.77	1.0	1.0
ViT	Last layer	0.97	0.96	1.0	0.88	0.97	0.83	0.99	0.9	0.86	0.47	1.0	1.0



Figure 23: PCX visualizations using latent relevances after the 3rd residual block of a ResNet50 model trained on ISIC2019 with the controlled microscope artifact (*left*), and after the 4th residual block of a ResNet50 model trained on the clean ISIC2019 data (*right*). For the former, only samples from the attacked class “melanoma” are considered, and for the latter we use samples from class “melanocytic nevus”. Columns represent prototypes with four representative samples, rows represent concepts (visualized via RelMax) and the values in the matrix indicate the average relevance of the concept for the prototype. For the attacked data (*left*), **prototype 2** focuses on the inserted microscope artifact with high scores for the related concepts (neurons) #979 and #543. For the clean ISIC2019 data (*right*), interestingly, **prototype 0** focuses **red-colored skin** with high scores for the related concepts #1147 and #1737.

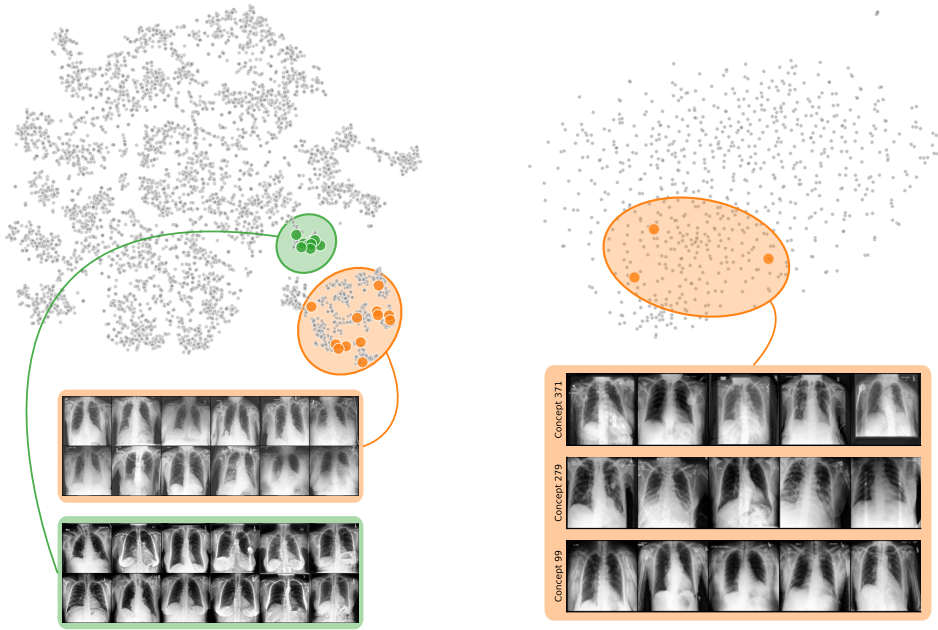


Figure 24: Artifact identification for a ViT model trained on CheXpert with the **brightness** artifact with samples from the “cardiomegaly”-class using relevances of the **class**-token on the last layer. We apply SpRAy on latent relevances for the data perspective (*left*) and pair-wise cosine similarities for the model perspective (*right*). Whereas the former reveals a clear cluster of samples with the **brightness** artifact, the latter does not lead to outlier concepts focusing on the artifact. Note that we highlight concepts for neurons #371, #279 and #99, as they are revealed as relevant for impacted samples via PCX in Fig. 25.

Table 6: Quantitative results for neuron-based biased sample retrieval w.r.t. the real-world artifacts **band-aid**, **ruler** (both ISIC2019), and **pacemaker** (CheXpert), as well as the controlled artifacts **microscope** (ISIC2019), **timestamp** (HyperKvasir), and **brightness** (CheXpert). We report AUROC and AP to evaluate the ranking capabilities of individual-neuron-based bias scores using activations on different layers of VGG16, ResNet50, and ViT models. Out of all neurons, the best performing neurons are selected on the validation set and results are reported for the unseen test set. Higher scores are better.

	layer	ISIC2019				HypKvasir		CheXpert					
		band-aid		ruler		timestamp		pacemaker		brightness			
		AUC	AP	AUC	AP	AUC	AP	AUC	AP	AUC	AP		
VGG16	Conv 4	0.98	0.44	0.91	0.31	0.98	0.86	0.84	0.29	0.64	0.08	0.56	0.04
	Conv 7	0.96	0.31	0.95	0.40	0.97	0.83	0.89	0.63	0.73	0.25	0.68	0.04
	Conv 10	0.94	0.29	0.97	0.68	0.98	0.88	0.94	0.52	0.91	0.52	0.82	0.12
	Conv 13	0.97	0.32	0.98	0.56	0.96	0.78	0.97	0.83	0.79	0.41	0.97	0.47
ResNet50	Block 1	0.99	0.85	0.90	0.24	0.60	0.17	0.98	0.82	0.80	0.13	0.90	0.73
	Block 2	1.00	0.89	0.94	0.52	0.77	0.29	0.98	0.85	0.88	0.22	0.89	0.59
	Block 3	1.00	0.90	0.99	0.70	0.76	0.26	0.97	0.83	0.94	0.20	1.00	0.92
	Block 4	1.00	0.86	0.99	0.65	0.87	0.54	0.98	0.88	0.99	0.95	0.96	0.90
ViT	Last layer	0.73	0.08	0.88	0.24	0.9	0.5	0.95	0.79	0.67	0.15	0.96	0.77

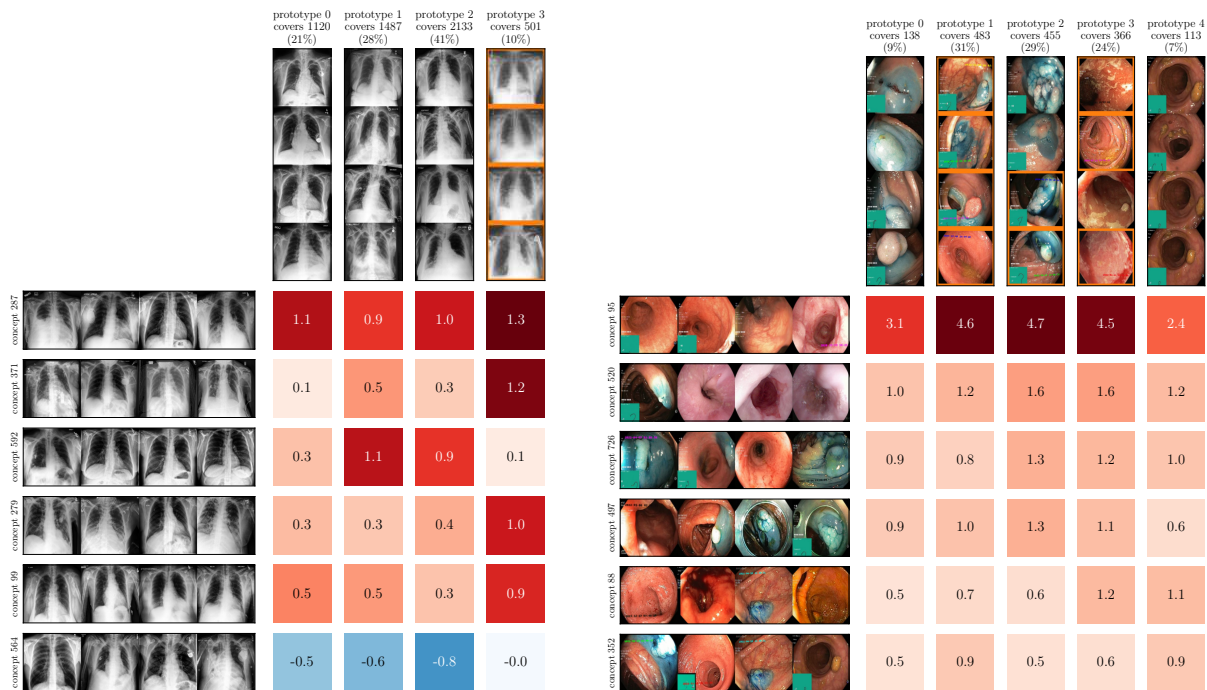


Figure 25: PCX visualizations using latent relevances for the `class`-token on the last layer of ViT trained on CheXpert with the controlled `brightness` artifact (*left*), and on HyperKvasir with the controlled `timestamp` artifact (*right*). Columns represent prototypes with four representative samples, rows represent concepts (visualized via RelMax) and the values in the matrix indicate the average relevance of the concept for the prototype. For the CheXpert (*left*), **prototype 3** focuses on the `brightness` artifact, with high scores for the related concepts (neurons) #371, #279 and #99. For HyperKvasir (*right*), no prototype primarily focuses on the artifact and clinically relevant features dominate.

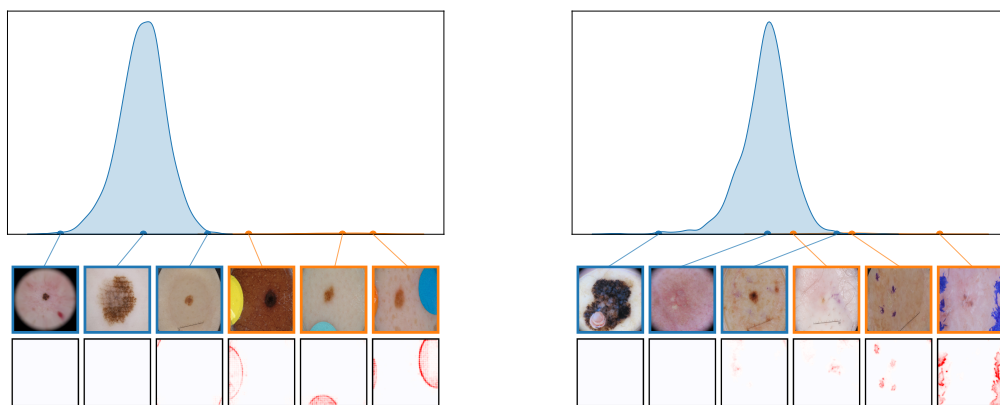


Figure 26: *Top*: Distribution of bias scores for real artifacts `band-aid` (*left*) and `skin-marker` (*right*) in the ISIC2019, split into unlabeled samples (*blue*) and samples labeled (*orange*) as artifact. *Bottom*: Samples at the 1-, 50-, and 99-percentile of each sample set and the artifact localization using the CAV. For `skin-marker`, the unlabeled sample in the 99-percentile is a false negative, i.e., although barely visible, it contains ink, and has not yet been detected in the data annotation process.

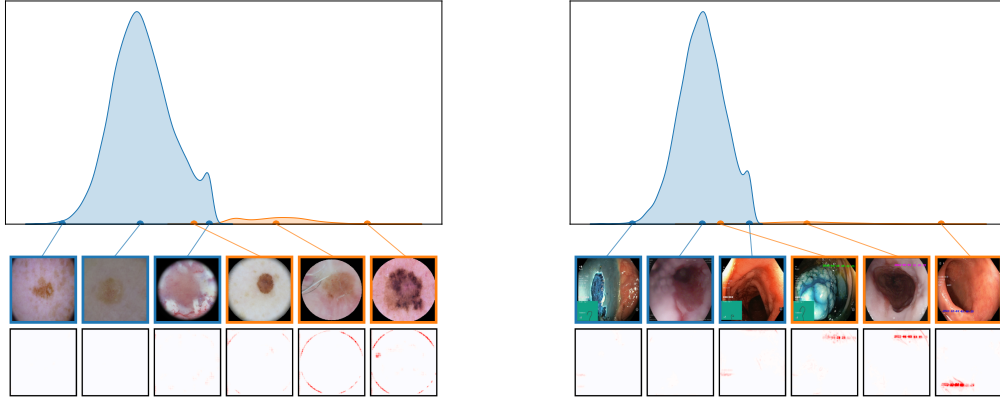


Figure 27: *Top*: Distribution of bias scores for controlled artifacts **microscope** in ISIC2019 (*left*) and **timestamp** in HyperKvasir (*right*), split into clean (*blue*) and manipulated (*orange*) samples. *Bottom*: Samples at the 1-, 50-, and 99-percentile of each sample set and the artifact localization using the CAV. The samples in the 99-percentile of the clean sets contain natural artifacts similar to the artificially inserted ones.

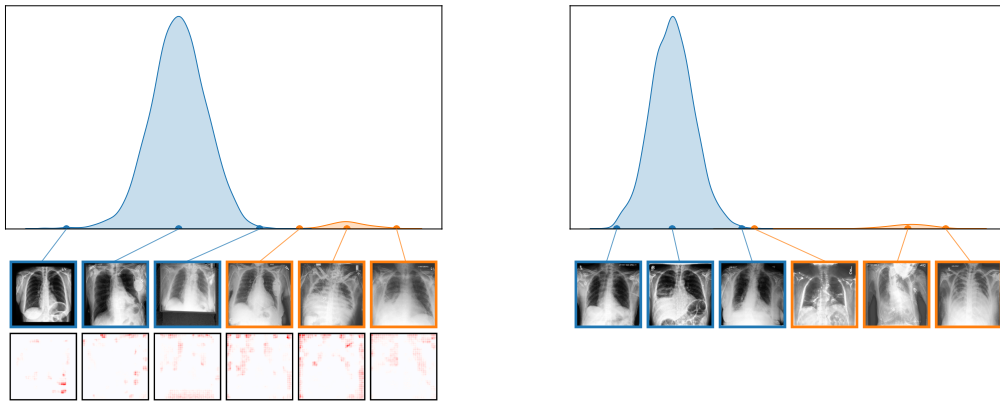


Figure 28: *Top*: Distribution of bias scores for the controlled **brightness** artifact in CheXpert for ResNet50 (*left*) and ViT (*right*), split into clean (*blue*) and manipulated (*orange*) samples. *Bottom*: Samples at the 1-, 50-, and 99-percentile of each sample set and the artifact localization using the CAV.

Table 7: Quantitative bias localization results for the controlled artifacts **microscope** (ISIC2019) and **timestamp** (HyperKvasir) with ground truth masks available. We report artifact relevance and IoU for computed bias localizations using CAVs in different layers of VGG16 and ResNet50 models. Higher scores are better.

model	layer	microscope (ISIC2019)		timestamp (HyperKvasir)	
		% relevance	IoU	% relevance	IoU
VGG16	Conv 4	0.50	0.14	0.18	0.26
	Conv 7	0.45	0.11	0.38	0.58
	Conv 10	0.45	0.11	0.53	0.60
	Conv 13	0.32	0.08	0.44	0.52
ResNet50	Block 1	0.55	0.16	0.28	0.42
	Block 2	0.49	0.12	0.63	0.68
	Block 3	0.48	0.09	0.74	0.65
	Block 4	0.40	0.04	0.69	0.58

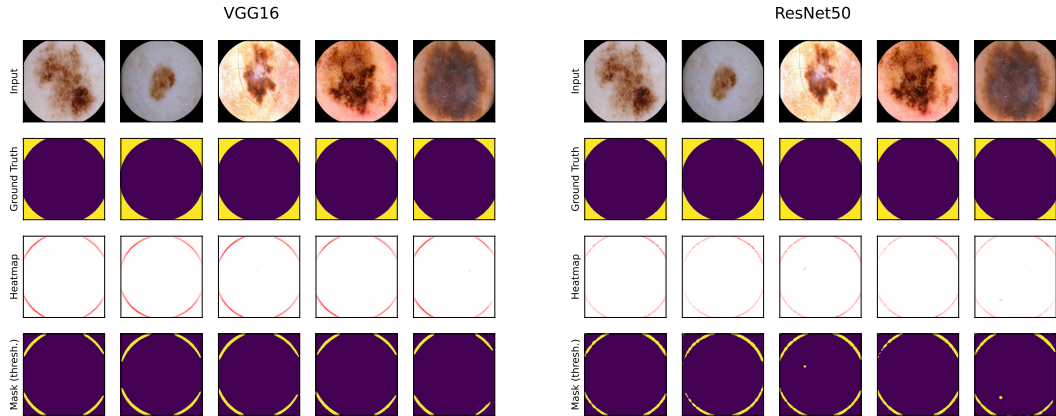


Figure 29: Examples for bias localization for the controlled `microscope` artifact in ISIC2019 using VGG16 (*left*) and ResNet50 (*right*) model architectures. We show the input samples (1st row), ground truth masks (2nd row), computed concept heatmaps using CAVs (3rd row), and binarized masks using Otsu’s method (4th row). Both models focus only on the border of the circle, instead of the entire area.

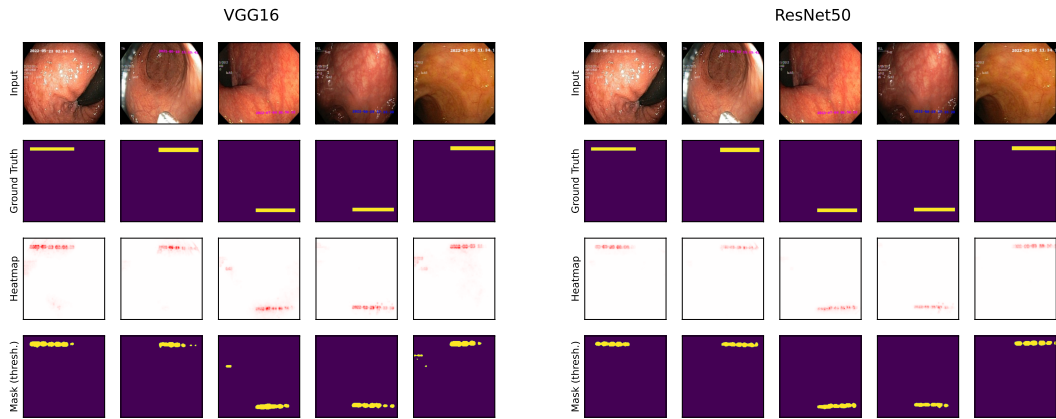


Figure 30: Examples for bias localization for the controlled `timestamp` artifact in HyperKvasir using VGG16 (*left*) and ResNet50 (*right*) model architectures. We show the input samples (1st row), ground truth masks (2nd row), computed concept heatmaps using CAVs (3rd row), and binarized masks using Otsu’s method (4th row).

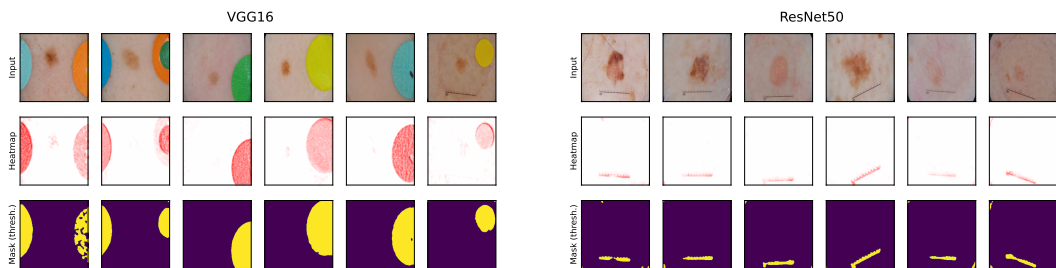


Figure 31: Examples for bias localization for the real-world artifacts `band-aid` (*left*) and `ruler` (*right*) in ISIC2019. The artifact concept is modeled using CAVs with activations after the 3rd conv layer of a VGG16 model for `band-aid` and after the 3rd residual block of a ResNet50 model for `ruler`. We show the input samples (1st row), computed concept heatmaps (2nd row), and binarized masks using Otsu’s method (3rd row).

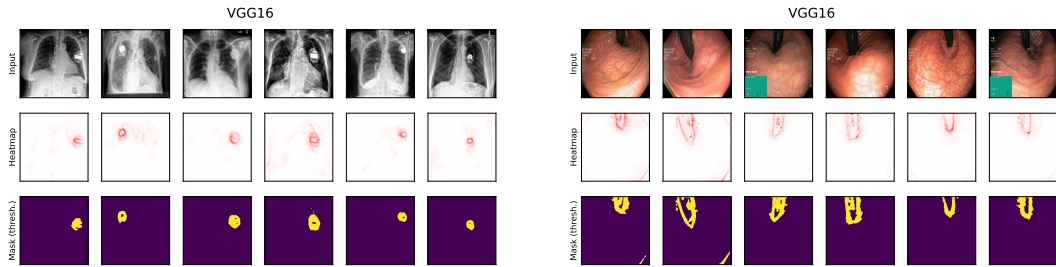


Figure 32: Examples for bias localization for the real-world artifacts **pacemaker** in CheXpert (*left*) and **insertion tube** in HyperKvasir (*right*). The artifact concept is modeled using CAVs with activations after the 10th and 13th conv layers of VGG16 models, respectively. We show input samples (1st row), concept heatmaps (2nd row), and binarized masks using Otsu’s method (3rd row).

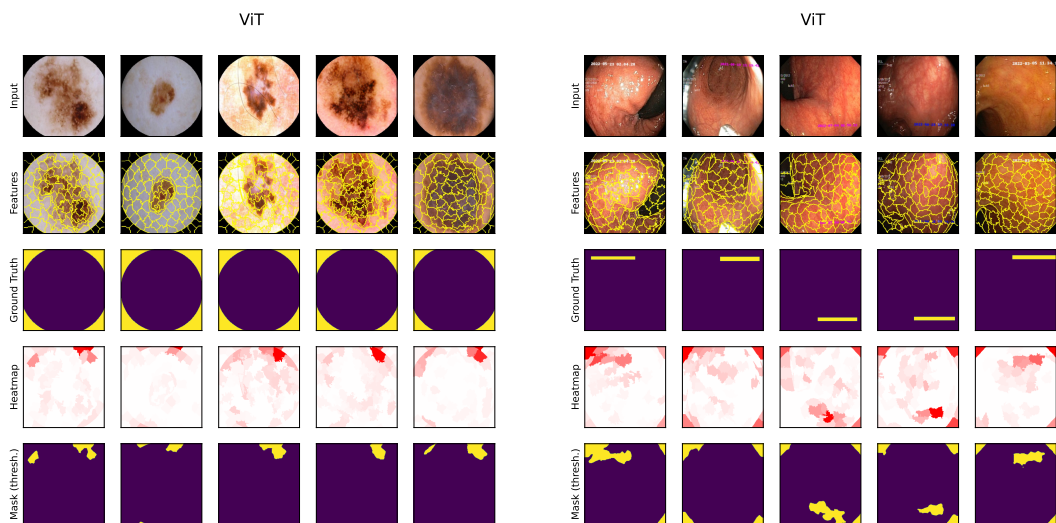


Figure 33: Examples for bias localization for the controlled artifacts **microscope** in ISIC2019 (*left*) and **timestamp** in HyperKvasir (*right*) using ViT models. The artifact concept is modeled using CAVs with activations in the last linear layer. SHAP [83] on superpixels computed via SLIC [81]. We show input samples (1st row), superpixels (2nd row), ground truth localization (3rd row), concept heatmaps (4th row), and binarized masks using Otsu’s method (5th row).

Table 8: Bias mitigation results with RRR, RR-ClArC, and P-ClArC (plain and reactive) for XResNet1d50 model for static noise as controlled spurious correlation in the PTB-XL dataset. We report accuracy and false positive rate (class: LVH) on a clean and biased test set, artifact relevance and Δ TCAV and arrows indicate whether high (\uparrow) or low (\downarrow) are better.

Method	Accuracy \uparrow		FPR (LVH) \downarrow		Art. rel. \downarrow	Δ TCAV \downarrow
	clean	biased	clean	biased		
<i>Vanilla</i>	0.96	0.94	0.00	0.43	0.48	0.06
RRR	0.96	0.95	0.00	0.32	0.57	0.06
RR-ClArC	0.96	0.96	0.00	0.09	0.26	0.09
P-ClArC	0.96	0.96	0.00	0.02	0.28	0.10
rP-ClArC	0.96	0.96	0.00	0.02	0.28	0.10

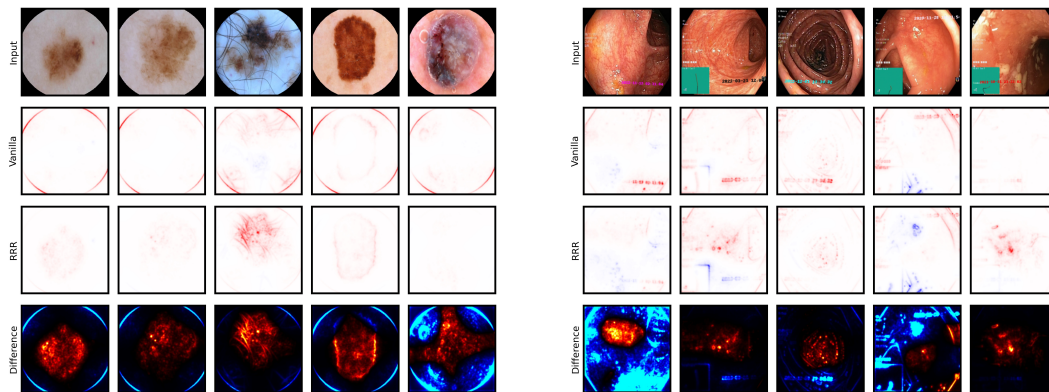


Figure 34: Local explanations, computed via LRP and presented as relevance heatmaps, without (*Vanilla*) and with (*RRR*) bias mitigation for the controlled versions of the ISIC2019 (*left*) and HyperKvasir (*right*) datasets. Red indicates a positive and blue a negative impact towards the predicted class. Whereas the Vanilla model is highly dependant on the inserted artifacts, *i.e.*, **microscope** for ISIC2019 and **timestamp** for HyperKvasir, the corrected model (RRR) shifts the relevance from the artifact to medically relevant features. We further plot a difference heatmap between the Vanilla and corrected (RRR) models, with red and blue indicating increased and decreased relevance, respectively.

Table 9: Bias mitigation results with RRR using computed heatmaps (hm), binarized versions (bin), and ground truth masks (gt), RR-ClArC, and P-ClArC (plain and reactive) for VGG16 models for controlled spurious correlations, specifically ISIC2019 (**microscope**) | HyperKvasir (**timestamp**) | CheXpert (**brightness**). We report accuracy on a clean and biased test set, artifact relevance and Δ TCAV and arrows indicate whether high (\uparrow) or low (\downarrow) are better.

Method	Accuracy (clean) \uparrow			Accuracy (biased) \uparrow			Art. relevance \downarrow			Δ TCAV \downarrow		
<i>Vanilla</i>	0.85	0.97	0.83	0.25	0.67	0.53	0.45	0.26	-	0.34	0.34	0.31
RRR (hm)	0.82	0.96	-	0.70	0.94	-	0.09	0.07	-	0.18	0.24	-
RRR (bin)	0.81	0.97	-	0.73	0.95	-	0.08	0.07	-	0.17	0.26	-
RRR (gt)	0.82	0.97	-	0.73	0.96	-	0.05	0.06	-	0.20	0.30	-
RR-ClArC	0.82	0.96	0.83	0.64	0.95	0.82	0.28	0.13	-	0.22	0.12	0.03
P-ClArC	0.42	0.78	0.77	0.58	0.88	0.78	0.21	0.07	-	0.27	0.05	0.13
rP-ClArC	0.84	0.97	0.83	0.59	0.89	0.78	0.21	0.07	-	0.27	0.05	0.13

Table 10: Bias mitigation results with RRR using computed heatmaps (hm), binarized versions (bin), and ground truth masks (gt), RR-ClArC, and P-ClArC (plain and reactive) for ResNet50 models for controlled spurious correlations, specifically ISIC2019 (**microscope**) | HyperKvasir (**timestamp**) | CheXpert (**brightness**). We report accuracy on a clean and biased test set, artifact relevance and Δ TCAV and arrows indicate whether high (\uparrow) or low (\downarrow) are better.

Method	Accuracy (clean) \uparrow			Accuracy (biased) \uparrow			Art. relevance \downarrow			Δ TCAV \downarrow		
<i>Vanilla</i>	0.87	0.97	0.81	0.28	0.62	0.44	0.55	0.51	-	0.17	0.30	0.33
RRR (hm)	0.87	0.97	-	0.44	0.77	-	0.55	0.48	-	0.16	0.29	-
RRR (bin)	0.87	0.97	-	0.43	0.76	-	0.54	0.46	-	0.16	0.29	-
RRR (gt)	0.84	0.97	-	0.51	0.82	-	0.53	0.45	-	0.19	0.30	-
RR-ClArC	0.86	0.97	0.82	0.76	0.96	0.79	0.42	0.34	-	0.00	0.07	0.00
P-ClArC	0.82	0.83	0.72	0.59	0.92	0.76	0.44	0.18	-	0.07	0.11	0.30
rP-ClArC	0.87	0.97	0.81	0.60	0.92	0.76	0.42	0.19	-	0.07	0.11	0.30

Table 11: Bias mitigation results with RRR using ground truth masks (gt), RR-ClArC, and P-ClArC (plain and reactive) for ViT models for controlled spurious correlations, specifically ISIC2019 (microscope) | HyperKvasir (timestamp) | CheXpert (brightness). We report accuracy on a clean and biased test set, artifact relevance computed and Δ TCAV and arrows indicate whether high (\uparrow) or low (\downarrow) are better.

Method	Accuracy (clean) \uparrow			Accuracy (biased) \uparrow			Art. relevance \downarrow			TCAV _{sens} \downarrow		
<i>Vanilla</i>	0.81	0.93	0.80	0.27	0.42	0.25	0.16	0.21	-	1.47	0.45	0.38
RRR (gt)	0.77	0.92	-	0.59	0.54	-	0.07	0.12	-	0.24	0.14	-
RR-ClArC	0.81	0.93	0.80	0.31	0.42	0.31	0.14	0.21	-	0.00	0.00	0.00
P-ClArC	0.81	0.93	0.80	0.30	0.43	0.32	0.14	0.21	-	0.42	0.04	0.16
rP-ClArC	0.81	0.93	0.80	0.30	0.42	0.32	0.14	0.21	-	0.42	0.04	0.16

Table 12: Chosen λ values for bias mitigation runs with RRR and RR-ClArC for our controlled experiments with the datasets HyperKvasir, ISIC2019, CheXpert, and PTB-XL. We selected the best performing values on the validation set and report results on an unseen test set.

Approach	HyperKvasir			ISIC2019			CheXpert			PTB-XL
	VGG	ResNet	ViT	VGG	ResNet	ViT	VGG	ResNet	ViT	XResNet
RRR (hm)	$5 \cdot 10^3$	$5 \cdot 10^4$	-	$5 \cdot 10^3$	$5 \cdot 10^5$	-	-	-	-	-
RRR (bin)	$5 \cdot 10^3$	$5 \cdot 10^4$	-	10^4	$5 \cdot 10^5$	-	-	-	-	-
RRR (gt)	10^3	$5 \cdot 10^4$	$5 \cdot 10^2$	10^4	10^5	10^4	-	-	-	$5 \cdot 10^3$
RR-ClArC	$5 \cdot 10^9$	10^9	10^1	10^{10}	$5 \cdot 10^9$	10^1	10^{10}	$5 \cdot 10^{12}$	$5 \cdot 10^1$	$5 \cdot 10^3$

Additional References Appendix

- [81] Radhakrishna Achanta, Appu Shaji, Kevin Smith, Aurelien Lucchi, Pascal Fua, and Sabine Süsstrunk. Slic superpixels compared to state-of-the-art superpixel methods. *IEEE TPAMI*, 34(11):2274–2282, 2012.
- [82] Corinna Cortes and Vladimir Vapnik. Support-vector networks. *Machine learning*, 20:273–297, 1995.
- [83] Scott M Lundberg and Su-In Lee. A unified approach to interpreting model predictions. *NeurIPS*, 30, 2017.
- [52] W James Murdoch, Peter J Liu, and Bin Yu. Beyond word importance: Contextual decomposition to extract interactions from lstms. *ICLR*, 2018.
- [85] Shauli Ravfogel, Yanai Elazar, Hila Gonen, Michael Twiton, and Yoav Goldberg. Null it out: Guarding protected attributes by iterative nullspace projection. In Dan Jurafsky, Joyce Chai, Natalie Schluter, and Joel Tetreault, editors, *ACL*, pages 7237–7256, July 2020.
- [86] Shibani Santurkar, Dimitris Tsipras, Mahalaxmi Elango, David Bau, Antonio Torralba, and Aleksander Madry. Editing a classifier by rewriting its prediction rules. *NeurIPS*, 34:23359–23373, 2021.